Predicting the Bifurcation Structure of Localized Snaking Patterns

Elizabeth Makrides*
Division of Applied Mathematics
Brown University
Providence, RI 02912, USA

Björn Sandstede
Division of Applied Mathematics
Brown University
Providence, RI 02912, USA

September 6, 2013

Abstract

We expand upon a general framework for studying the bifurcation diagrams of localized spatially oscillatory structures. Building on work by Beck *et al.*, the present work provides rigorous analytical results on the effects of perturbations to systems exhibiting snaking behavior. Starting with a reversible variational system possessing an additional $\mathbb{Z}_2$ symmetry, we elucidate the distinct effects of breaking symmetry and breaking variational structure, and characterize the resulting changes in both the bifurcation diagram and the solutions themselves. We show how to predict the branch reorganization and drift speeds induced by any particular given perturbative term, and illustrate our results via numerical continuation. We further demonstrate the utility of our methods in understanding the effects of particular perturbations breaking reversibility. Our approach yields an analytical explanation for previous numerical results on the effects of perturbations in the one-dimensional cubic-quintic Swift–Hohenberg model, and allows us to make predictions on the effects of perturbations in more general settings, including planar systems. While our numerical results involve the Swift–Hohenberg model system, we emphasize the general applicability of the analytical results.

Keywords Bifurcation; Homoclinic snaking; Localized structures; Planar patterns; Swift–Hohenberg equation

1 Introduction

Localized structures, in which a spatially oscillatory pattern on a finite spatial range connects to a trivial homogeneous solution outside this range, have been observed in numerous physical systems [1, 4, 5, 11, 19]; see also [2, 13] for additional references. The bifurcation diagrams of such patterns often exhibit snaking behavior, in which a branch of symmetric solutions winds back and forth between two limits of an appropriate parameter, allowing for patterns of arbitrary spatial extent [8, 10, 14, 20, 21, 24]. Asymmetric solution branches connecting symmetric snaking branches were discovered numerically in [8], using the Swift–Hohenberg model system in one dimension. The origin of the symmetric and asymmetric solution branches was explained under general hypotheses in [3], and near a certain codimension-two point in [9].

One characteristic common to many snaking systems is spatial reversibility. Often, such systems are also variational, and some are invariant under an additional $\mathbb{Z}_2$ symmetry corresponding, for example, to symmetry in the midplane of a fluid system. The snaking diagrams in reversible, variational systems with or without additional $\mathbb{Z}_2$ symmetry are now generally well understood. Of interest is then how the structure of snaking diagrams changes when reversibility, variational structure, or $\mathbb{Z}_2$ symmetries, if present, are broken, either individually or jointly,

*elizabeth_makrides@brown.edu; T: +1 401 863-3113; F: +1 401 863-1355

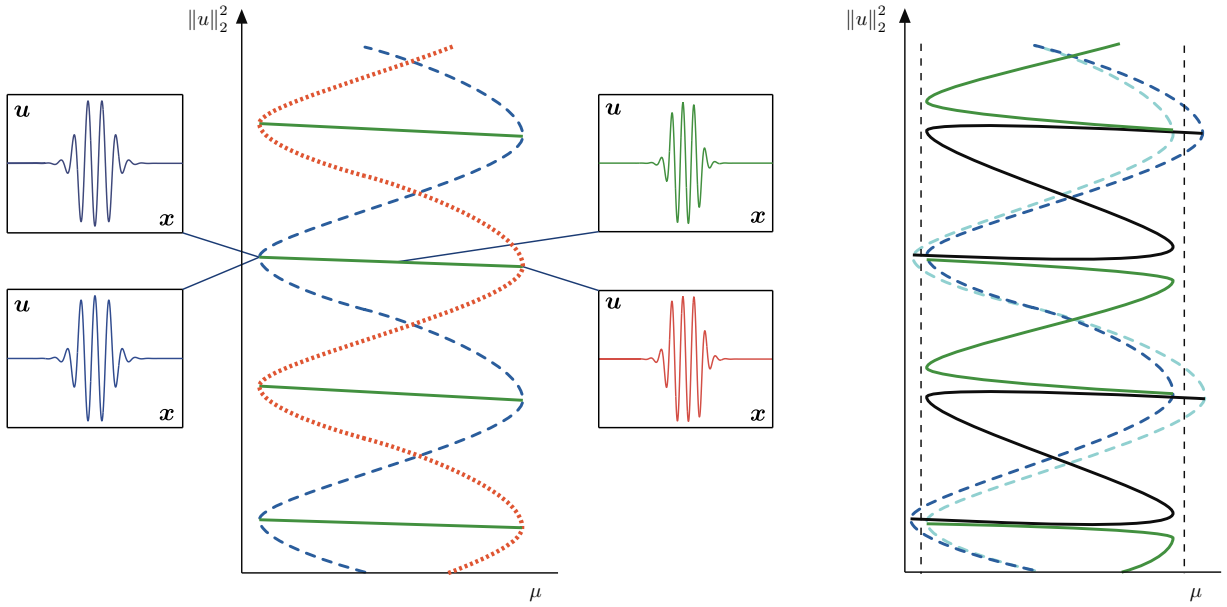

Figure 1: Left: *Schematic of the bifurcation diagram for the unperturbed system (1.2) with $\varepsilon = 0$, with illustrative solution profiles. The dashed dark blue snaking branch consists of two branches of even parity solutions, while the dotted orange branch consists of two branches of odd parity solutions. Solid green cross-connecting branches consist of four sets of asymmetric solutions.* Right: *Schematic of the bifurcation diagram for a perturbed system as in (1.2) with $\varepsilon \neq 0$. Snaking branches for even symmetric patterns with central maximum and minimum are shown in dark and light blue dashed, respectively. Asymmetric branches are in solid black and green. Dashed vertical lines indicate the saddle node locations from the unperturbed system.*

by adding perturbative terms to the governing equation. The effects of breaking reversibility were recently explored analytically in [7, 16, 22], while numerical studies of perturbations that break variational structure and $\mathbb{Z}_2$ symmetry were carried out recently in [15]. Generally speaking, breaking reversibility or symmetry leads to a rearrangement of bifurcation branches, while breaking the variational structure leads to patterns that drift with nonzero speed.

In this manuscript, we follow up on the results of [3] to show that perturbative terms breaking symmetry or variational structure affect solution profiles and overall bifurcation structure in ways which are fully predictable analytically. By evaluating scalar products involving only solutions of the unperturbed system and perturbative terms evaluated at unperturbed solutions, we are able to predict which of many topologically distinct bifurcation diagrams will emerge upon introduction of perturbative terms, as well as the drift speeds of asymmetric solutions where appropriate. We confirm these predictions numerically for various perturbations to the cubic-quintic Swift–Hohenberg system both on the line and in the plane. Though we use the Swift–Hohenberg equation to demonstrate our results numerically, we wish to emphasize that our results are not specific to the Swift–Hohenberg setting.

To illustrate snaking and to motivate the questions addressed in this paper, we review results on snaking for the one-dimensional cubic-quintic Swift–Hohenberg equation given by

$$u_t = -(1 + \partial_x^2)^2 u - \mu u + \nu u^3 - u^5, \tag{1.1}$$

which has been studied extensively in the pattern formation literature. The system (1.1) is reversible under $x \mapsto -x$, equivariant under the $\mathbb{Z}_2$ symmetry $u \mapsto -u$, and admits a variational structure. The left-hand side of Figure 1 provides a schematic of its bifurcation diagram, along with sample solution profiles. We note that the snaking branch in dashed dark blue consists of two solution branches lying on top of each other in the $(\mu, \|u\|_2^2)$ plane, one consisting of symmetric solutions with a central maximum and the other one of symmetric solutions

with a central minimum: these two solution profiles are transformed into each other by the symmetry $u \mapsto -u$. Similarly, the dotted orange snaking branch is actually two branches of odd parity solutions related again by the $u \mapsto -u$ symmetry. Finally, each asymmetric ladder branch is a set of four solution branches, which coincide in the $(\mu, \|u\|_2^2)$ plane. Moving up along a snaking branch, localized structures grow by increasing the extent of the spatially periodic region between the trivial homogeneous state.

The effect of perturbative terms added to (1.1) was recently explored numerically by Houghton and Knobloch [15]. In particular, Houghton and Knobloch examine[1] the variational system

$$u_t = -(1+\partial_x^2)^2 u - \mu u + \nu u^3 - u^5 + \varepsilon u^2 \tag{1.2}$$

as well as the non-variational system

$$u_t = -(1+\partial_x^2)^2 u - \mu u + \nu u^3 - u^5 + \varepsilon (\partial_x u)^2 \tag{1.3}$$

for $0 < \varepsilon \ll 1$. For $0 < \varepsilon \ll 1$, the systems no longer respect the symmetry $u \mapsto -u$, and the right-hand side of Figure 1 provides a schematic of the resulting bifurcation diagram for (1.2) with $\varepsilon \neq 0$. Houghton and Knobloch observe that the even solutions persist along unbroken snaking branches; however, in contrast to the $\varepsilon = 0$ case, the two snaking branches for the even symmetric solutions with, respectively, a central maximum and a central minimum no longer lie on top of each other due to the broken $\mathbb{Z}_2$ symmetry. Alternate saddle nodes on the left and right are now offset to the inside and outside of the original branches, so that the resulting bifurcation diagram possesses four snaking limits. Meanwhile the odd solutions are destroyed, and two types of asymmetric solution branches are formed, termed S and Z branches in accordance with their shapes. The Z branches start and end on the same symmetric branch, whereas the S branches connect the two symmetric solution branches to each other.

As outlined above, our goal is to explain the effects of breaking variational structure and $\mathbb{Z}_2$ symmetry rigorously and to predict branch rearrangement and drift speeds of patterns using solutions of the unperturbed system only. This paper is organized as follows: in Section 2, we link the framework introduced in [3] with a formal gluing approach of fronts and backs, first to indicate the broad applicability of the approach taken in [3] and, second, to understand some of the major features observed in systems admitting localized patterns. We note that this section is intended to provide intuition and motivate the particular hypotheses employed in the following section, rather than to present precise results for a particular system. In Section 3, we detail predictions on the evolution of bifurcation diagrams upon the introduction of perturbative symmetry breaking terms. In Section 4, we derive conditions that allow us to predict bifurcation diagrams and drift speeds upon adding perturbative terms to the underlying system; these conditions rely on evaluation of the perturbative terms along solutions of the unperturbed system. Specifically, in Section 4.1, we detail the effects of perturbative terms breaking variational structure; in Section 4.2, we show how to use our earlier results to make predictions for specific perturbations breaking $\mathbb{Z}_2$ symmetry; and in Section 4.3, we show how our methods may be employed to anticipate which of two types of bifurcation diagram emerges upon the introduction of nonreversible terms, where the two types have been identified previously in [16, 22]. In Section 5, we provide numerical studies supporting our analytical results using the 1D and 2D Swift–Hohenberg equations. Finally, the discussion in Section 6 identifies areas for future work.

2 General framework

Our aim in this section is to relate the rigorous analysis and its underlying framework developed in [3] with a formal approach that views the emergence of localized roll patterns via gluing together appropriate building

[1] We remark that Houghton and Knobloch use the bifurcation parameter $r := -\mu$ instead of μ: hence, their bifurcation diagrams are flipped in comparison to ours; in our description of their results, we use μ as the parameter.

blocks consisting of fronts and backs. Outlining this connection should indicate the broad applicability of the results in [3] without expanding on the technical account in that paper. The link between these two different approaches will also enable us to predict the effects of perturbations more easily in the forthcoming sections.

2.1 System structure

We will begin by assuming three properties of our system: first, that it is reversible, i.e., possesses $x \mapsto -x$ symmetry, with $x \in \mathbb{R}$, so that if $u(x) \in \mathbb{R}^n$ is a solution, so is $u(-x)$. Second, we assume it possesses a $\mathbb{Z}_2$ symmetry κ, which for simplicity we take to be $\kappa : u \mapsto -u$, so that if $u(x)$ is a solution, so is $-u(x)$. Third, we assume that the system is variational and can be written as

$$u_t = -\nabla \mathcal{E}(u) \tag{2.1}$$

with

$$\mathcal{E}(u) = \int_{\mathbb{R}} \mathcal{L}(u(x), u_x(x), u_{xx}(x))dx$$

(or, more generally, $\mathcal{L} = \mathcal{L}(u, u_x, \ldots, \partial_x^n u)$ for some n). The existence of a variational structure implies that if $u(x-ct)$ is a localized solution to (2.1), then necessarily $c = 0$ (see Section 4.1 below). The variational structure also implies the existence of a spatial Hamiltonian H that is conserved pointwise along any solution $u(x)$ of the steady state equation $-\nabla \mathcal{E}(u) = 0$; see, for example, [17].

2.2 Wave trains, fronts and backs

We next assume that our system possesses wave trains, that is, spatially oscillatory solutions with nonzero minimal period. Spatial reversibility implies that wave trains should come in a one-parameter family, which we take to be parameterized by the variable e, with spatial periods $p(e)$. We refer to this family as $v(x, e)$, and assume that each member of the family is invariant under $x \mapsto -x$. Whenever the symmetry $\kappa : u \mapsto -u$ is present in our system, we will assume that $v(x, e)$ is compatible with this symmetry for each e so that $v(-x, e) = -v(x, e)$. Finally, for variational systems, the wave trains will generically be parameterized by $e = H$, the value of the spatial Hamiltonian evaluated along the wave train.

We make the further assumption that the system admits fronts, i.e., solutions evolving from a constant state to a spatially oscillatory one. More precisely, we assume that there exist steady states $u_f(x)$ such that $u_f(x) \to u_0$ as $x \to -\infty$ and $u_f(x) \to v(x)$ as $x \to +\infty$, where $v(x)$ is a member of the family $v(x, e)$. Assuming that $H(u_0) = 0$, the selected periodic solution $v(x)$ will satisfy $e = H = 0$. We note that we can rescale x so that $p(0) = 2\pi$.

In fact, we can more generally consider systems admitting solutions $u_f(x, y)$, where $y \in \Omega \Subset \mathbb{R}^{d-1}$, which satisfy $u_f(x, y) \to w(y)$ as $x \to -\infty$, where $w(y)$ is any function independent of x, as well as $u_f(x, y) \to v(x, y)$ as $x \to +\infty$, where $v(x, y)$ is periodic in x. In essence we require only that the evolution in space occur along one dimension, perhaps after an appropriate coordinate transformation. For simplicity in this section we write solutions as $u(x)$, but in subsequent sections we will use the more general formulation to predict some interesting effects of symmetry breaking, including the formation of isolas in planar systems under appropriate conditions, and to verify these predictions numerically.

In the case that $u_f(x)$ is a front, $u_b(x) := u_f(-x)$ exists by reversibility, and is termed a back; see Figure 2. Since we have assumed that the limiting oscillatory solution $v(x)$ is compatible with the κ symmetry, given a front solution $u_f(x)$ we will also have the front solution $u_{f2}(x) := -u_f(x)$, as well as the back solutions $u_{b1}(x) := u_f(-x)$ and $u_{b2}(x) := -u_f(-x)$.

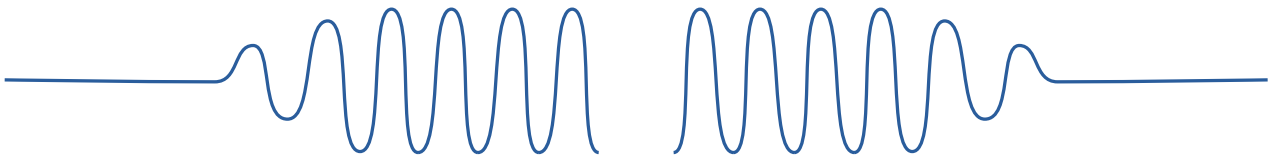

$u_f(x)$, a front $\qquad\qquad$ $u_b(x) = u_f(-x)$, a back

Figure 2: *Illustration of a front and a back, related by $x \mapsto -x$.*

2.3 Symmetric localized solutions: construction via "gluing"

We now wish to "glue" together front and back solutions to form a localized stationary solution $u_{loc}(x)$ which is invariant under $u(x) \mapsto u(-x)$. Clearly this is only possible if we have a maximum or minimum at the center of the localized oscillatory structure. Defining the phase φ at the center of the localized solution to be the distance traveled past a maximum, and rescaling x if necessary so that the spatially oscillatory limiting solution $v(x)$ mentioned above has period 2π, this is equivalent to requiring that the phase at the center of the structure satisfies $\varphi = 0$ or $\varphi = \pi$; see Figure 3.

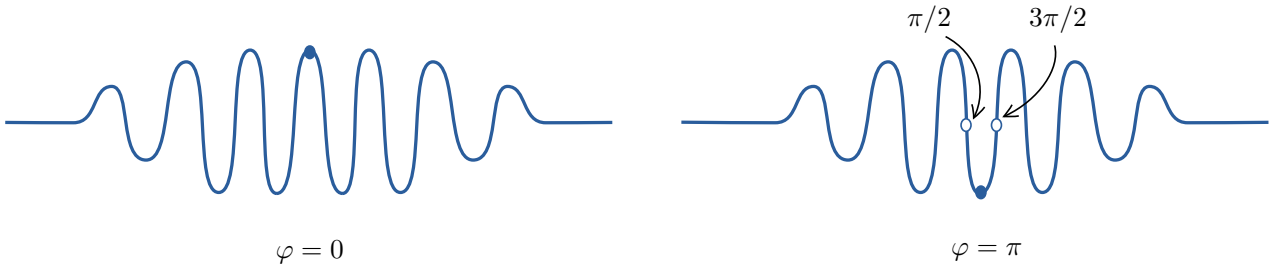

Figure 3: *Possible phases $\varphi = 0, \pi$ for a localized solution invariant under $x \mapsto -x$. The closed circles indicate the midpoint of the pattern, while the labels $\frac{\pi}{2}$ and $\frac{3\pi}{2}$ indicate the value of φ at the open circles.*

In the case that we have the additional symmetry $\kappa : u \mapsto -u$, compatibility of the 2π-periodic solution v_x with κ implies that $-v(x) = v(x + \pi)$, and we recall that the existence of a front solution $u_f(x)$ implies the existence of the front solution $u_{f2}(x) := -u_f(x)$ and the back solutions $u_{b1}(x) := u_f(-x)$ and $u_{b2}(x) := -u_f(-x)$. Thus we can form solutions invariant under $u(x) \mapsto -u(-x)$ by gluing a front $u_f(x)$ to a back $u_{b2} = -u_f(-x)$ with phase $\varphi = \frac{\pi}{2}$ or $\varphi = \frac{3\pi}{2}$; see Figure 4.

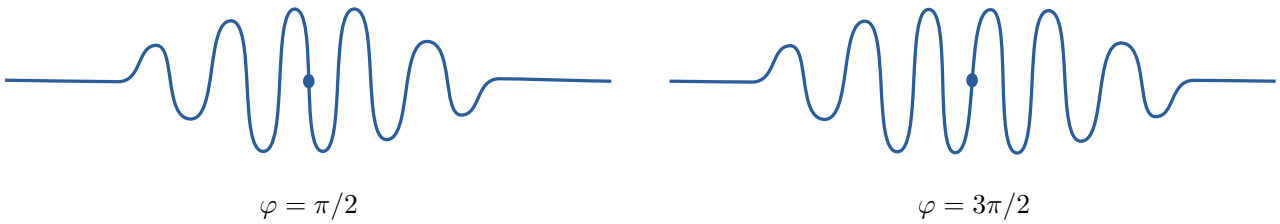

Figure 4: *Solutions invariant under $u(x) \mapsto -u(-x)$, with phases $\varphi = \frac{\pi}{2}, \frac{3\pi}{2}$.*

Moving forward, we will refer to solutions invariant under $u(x) \mapsto u(-x)$ as symmetric, or $\mathcal{R}$-symmetric. In the case that the system possesses the additional $\kappa : u \mapsto -u$ symmetry, we will also refer to solutions invariant

under $u(x) \mapsto -u(-x)$ as symmetric, or $\kappa\mathcal{R}$-symmetric. Any localized solution which is not invariant under either of these operations will be called asymmetric.

2.4 Solution lengths and parameter dependence

To this point, we have not considered the role of parameters in our system. If we only had one "type" of front present, which is to say all front solutions could be mapped to each other via a translation in x, then we would only be able to get symmetric localized states in lengths of multiples of 2π (or, if $u \mapsto -u$ symmetry is present, in multiples of π); see Figure 5. If, however, we can define a characteristic length of fronts such that the length of the fronts present in our system varies continuously with a parameter, then our system will typically admit localized symmetric solutions of arbitrary length via parameter variation.

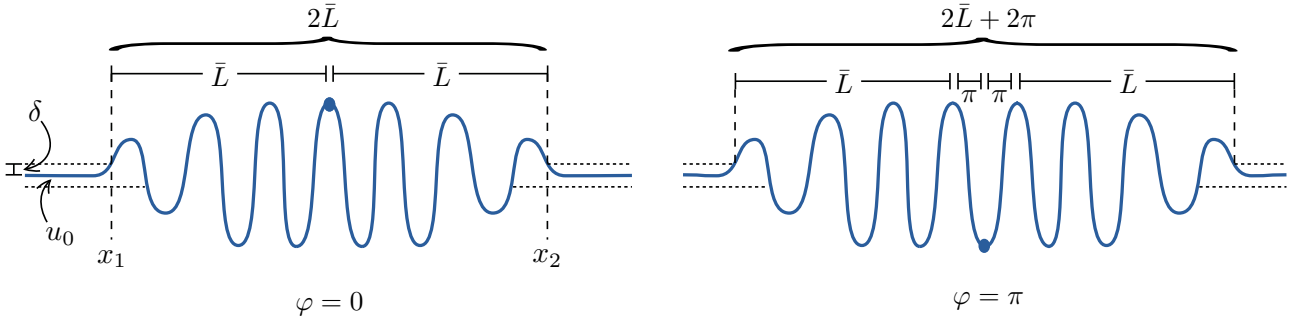

Figure 5: *The length of a localized structure, measured as the distance between the largest x, labeled x_1, such that $|u(x) - u_0| < \delta$ for all $x < x_1$, and the smallest x, labeled x_2 such that $|u(x) - u_0| < \delta$ for all $x > x_2$, for some fixed tolerance δ.*

We pause here to consider the notion of length. Although there is a natural and rigorous way to measure these lengths in a dynamical systems setting, using Poincaré sections near the oscillatory solution, we will not aim at fully rigorous definitions and instead suggest an approximate measurement using only the solution profiles. Specifically, we will make use of two distinct lengths: first, the *length of a localized structure* is the extent of the region where our localized solution lies near the oscillatory solution. We will generally denote this by $2\bar{L}$, since we are usually interested in half this length. To measure the length of a localized oscillatory solution, we can look at the difference between the largest x, called x_1 in Figure 5, such that $u_{loc}(x)$ is within some tolerance of the constant solution, and the smallest x, called x_2 in Figure 5, such that it is again within this tolerance. Alternatively, assuming $u_0 = 0$, we can use the L^2 norm of the whole localized solution. The former measurement is more natural for theoretical development, while the latter is more convenient for numerically computed bifurcation diagrams, but fundamentally both capture the same information.

Second, the *characteristic length of a front*, which we denote by l and define modulo 2π, corresponds to the length of the interface region between the constant and oscillatory solution measured to a peak, modulo 2π[2]. That is, we look at the difference between the largest x such that $u_{loc}(x)$ is within some tolerance of the constant solution to the smallest x corresponding to a peak (i.e., $u'(x) = 0$, $u''(x) < 0$) within some tolerance of the amplitude of the limiting oscillatory solution $v(x)$; see Figure 6. Again, assuming $u_0 = 0$, we can also measure this via the L^2 norm of the portion of a front lying to the left of an oscillatory peak within some tolerance of the maximum amplitude.

[2]Note that we are assuming all fronts connect to oscillatory solutions with the same period, which we normalize without loss of generality to 2π. In the case that the underlying periods of the oscillatory are distinct, we can rescale x in a μ-dependent fashion to ensure that each has period 2π.

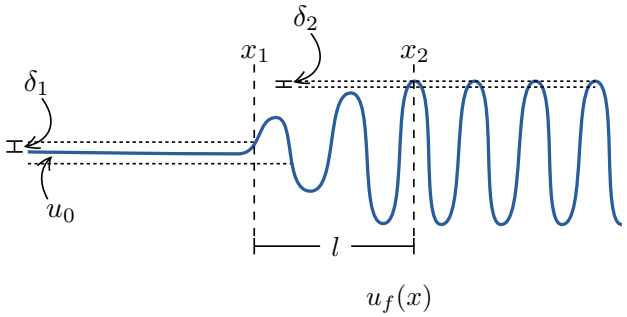

Figure 6: *The characteristic length of a front for some fixed tolerances δ_1 and δ_2, measured as the distance between the largest x, labeled x_1, such that $|u(x) - u_0| < \delta_1$ for all $x < x_1$, and the smallest x, labeled x_2, such that $u'(x_2) = 0$, $u''(x_2) < 0$, and $|u(x_2) - v(x_*)| < \delta_2$, where $v(\cdot)$ is the limiting oscillatory solution, and $v(x_*)$ has phase $\varphi = 0$.*

Having established these two types of length, and approximately how to measure them, we finally wish to include dependence on a system parameter μ. In general, fronts will come locally in branches (smooth solution curves) as the only steady-state bifurcations they typically undergo in 1-parameter systems are saddle node bifurcations (possibly after ignoring bifurcations caused by symmetry breaking in the transverse y-direction.) If we assume that fronts exist only for $\mu \in (\mu_1, \mu_2)$, then plotting (μ, l) along the branch of fronts, we obtain typical bifurcation or existence diagrams as shown in Figure 7. On the cylinder $(\mu_1, \mu_2) \times S^1$ (recall the characteristic length l of fronts is taken modulo 2π), the connected branch containing our front solution can have any one of these forms, as well as others not shown in Figure 7.

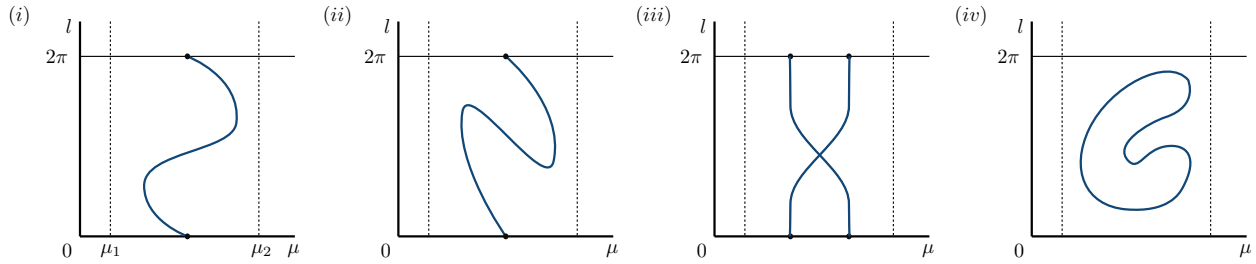

Figure 7: *Typical bifurcation and existence diagrams for fronts on $(\mu_1, \mu_2) \times S^1$, where l is the characteristic length of fronts and μ is a system parameter.*

Though the approach outlined below applies to all of these, we will assume for the sake of clarity that each l corresponds to a unique μ, so that the branch on $(\mu_1, \mu_2) \times S^1$ can be written as $\mu = z(l)$ with $l \in [0, 2\pi]/\sim$ for some function z, as illustrated in Figure 7(i). We can extend the function z to all of $\mathbb{R}$ by considering the argument modulo 2π. We will generally write $z(L)$ to indicate the extended version.

2.5 Bifurcation structure of localized solutions without additional symmetry

Now suppose we have a symmetric localized structure of length $2\bar{L}$ with maximum in the center, i.e., with phase $\varphi = 0$. Such a structure may be formed from a front of characteristic length $l = \bar{L} \bmod 2\pi$ and a back of the same characteristic length, so that such a solution exists for $\mu = z(\bar{L})$. On the other hand, a symmetric localized structure of length $2\bar{L}$ with minimum in the center (phase $\varphi = \pi$) is formed from a front of characteristic length $(\bar{L} - \pi) \bmod 2\pi$ and a back of characteristic length $(\bar{L} + \pi) \bmod 2\pi$, so that such a solution exists for $\mu = z(\bar{L} + \pi)$; recall here that z is 2π-periodic so that $z(\bar{L} + \pi) = z(\bar{L} - \pi)$. Consequently, in a bifurcation

diagram displaying the length (L^2 norm) of a localized solution versus parameter μ, the curve $\mu = z(\bar{L})$ will be the branch of symmetric localized solutions with maxima in the center, while the branch of solutions with minima in the center will be given by $\mu = z(\bar{L} + \pi)$. The resulting bifurcation diagram of symmetric branches for z as given in Figure 7(i) therefore consists of snaking branches which are intertwined in the sense of Figure 1.

Turning to asymmetric solutions, suppose we have a localized structure of length $2\bar{L}$, and again define the phase φ at the midpoint to be the distance past the nearest maximum on the left. Such a structure is formed from a front of characteristic length $(\bar{L} - \varphi) \bmod 2\pi$ and a back of characteristic length $(\bar{L} + \varphi) \bmod 2\pi$; see Figure 8.

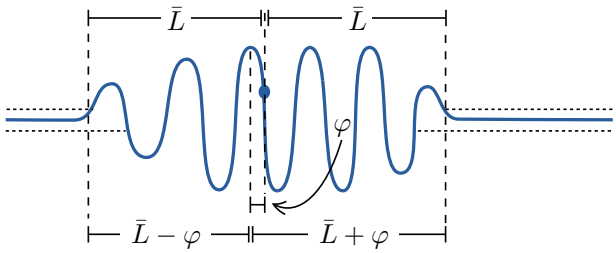

Figure 8: *An asymmetric localized structure of length $2\bar{L}$, which can be viewed as the result of combining a front of characteristic length $\bar{L} - \varphi$ with a back of characteristic length $\bar{L} + \varphi$, where φ is the phase at the midpoint of the localized structure.*

Thus we can have a localized structure of length $2\bar{L}$ and phase φ if and only if $\mu = z(\bar{L} + \varphi)$ and $\mu = z(\bar{L} - \varphi)$, requiring in particular that $z(\bar{L} + \varphi) = z(\bar{L} - \varphi)$. In other words, a localized structure of length $2\bar{L}$ can exist at a particular μ if and only if there exists a φ such that $\mu = z(\bar{L} + \varphi) = z(\bar{L} - \varphi)$. Of course, if we have a localized structure $u(x)$ of length $2\bar{L}$ for some μ, we will also have a localized structure $u(-x)$ with length $2\bar{L}$ at this μ, so that in a bifurcation diagram plotting solution length or norm vs. μ, every point along a branch of asymmetric solutions will correspond to two separate asymmetric solutions related by $x \mapsto -x$. This can also be understood by noting that if $u(x)$ has phase φ, $u(-x)$ will have phase $\tilde{\varphi} = 2\pi - \varphi$, so that by virtue of the 2π-periodicity of z, $\mu = z(\bar{L} + \tilde{\varphi}) = z(\bar{L} - \tilde{\varphi})$ will be satisfied.

In summary, all solution branches can be found by determining the values of L and φ such that

$$Z(L, \varphi) := z(L + \varphi) - z(L - \varphi) = 0. \tag{2.2}$$

The corresponding values of μ for which these solutions exist are determined by the relation $\mu = z(L + \varphi)$, which is of course equivalent to $\mu = z(L - \varphi)$ for all (L, φ) such that $Z(L, \varphi) = 0$. In particular, since z is 2π-periodic, we will have symmetric localized solutions for any L with $\varphi = 0$ or $\varphi = \pi$, whereas asymmetric solutions will exist for particular values of L and $\varphi \notin \{0, \pi\}$ satisfying $Z(L, \varphi) = 0$. The resulting bifurcation diagram of symmetric and asymmetric branches, for z as given in Figure 7(i), is therefore as shown in Figure 1: to understand the shape of the bifurcation branches, we needed only the existence of fronts, $x \mapsto -x$ symmetry, and a relationship between the length of the interface region of fronts and a system parameter.

We now connect the function z and the bifurcation equation (2.2), obtained here via formal gluing arguments, to the rigorous results established in [3]. In that paper, it was shown that symmetric and asymmetric branches correspond to solutions of a system of the form

$$Z(L, \varphi) + \mathrm{O}(e^{-KL}) = 0 \tag{2.3}$$

for some constant $K > 0$: in particular, for L large enough, regular zeros of (2.2) correspond to regular zeros of (2.3), and vice versa. In particular, under hypotheses detailed in [3], $\mathcal{R}$-symmetric solutions that spend time

$2L$ near the periodic orbit exist for points (μ, L) with $\mu = \mu_*(L, \varphi_0) = z(L + \varphi_0) + \mathrm{O}(e^{-KL})$ for some $K > 0$ with $\varphi_0 \in \{0, \pi\}$. Furthermore, all other single-pulse solutions that spend time $2L$ near the periodic orbit are exponentially close in L to the set of points (μ, L) such that $\mu = z(L + \varphi) = z(L - \varphi)$. Finally, it was shown in [3] that the function z appearing in (2.3) has a natural interpretation in terms of the intersection of invariant manifolds.

2.6 Bifurcation structure of localized solutions with $\mathbb{Z}_2$ symmetry

In the presence of a $\mathbb{Z}_2$ symmetry κ, the main distinction from the above is that the function z is now automatically π-periodic: supposing our symmetry to be $u \mapsto -u$, if a front $u(x)$ of length l exists at some parameter value μ, then a front $-u(x)$ with characteristic length $(l + \pi)$ mod 2π must also exist at this μ; see Figure 9.

Thus $z(l) = z(l+\pi)$ for all l, i.e., z is π-periodic. As a consequence, the bifurcation branch of symmetric solutions with maxima in the center will lie on top of those with minima in the center [$z(L) = z(L + \pi)$.] Moreover, the branches of $\kappa\mathcal{R}$-symmetric solutions with $\varphi = \frac{\pi}{2}$ or $\varphi = \frac{3\pi}{2}$ described previously will lie on top of each other for the same reason. Of course, the branches of the $\mathcal{R}$- and $\kappa\mathcal{R}$-symmetric solutions will be offset from each other by half a period, so that they have the appearance of being intertwined.

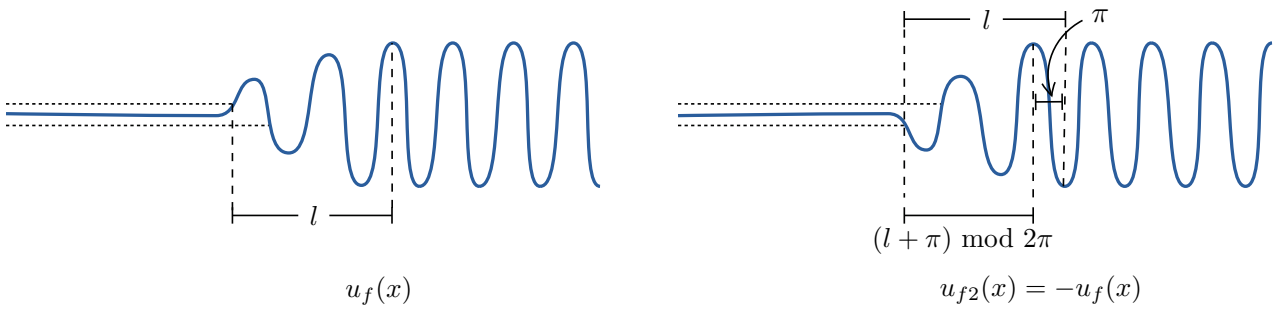

Figure 9: *Illustration that the function z will be π-periodic whenever the periodic orbit $v(x)$ respects both $x \mapsto -x$ and $u \mapsto -u$ symmetries.* Left: *A front $u_f(x)$ with characteristic length l, which we assume exists at some μ_0.* Right: *The front $u_{f2}(x) := -u_f(x)$ will also exist for this μ_0, and will have characteristic length $l + \pi$.*

Asymmetric solutions of length $2\bar{L}$ will again exist whenever we can satisfy $\mu = z(\bar{L} + \varphi) = z(\bar{L} - \varphi)$, keeping in mind that z is now π-periodic. Note that each point on a bifurcation branch of asymmetric solutions will now correspond to four such solutions: the "original" $u(x)$ plus $u(-x)$, $-u(x)$ and $-u(-x)$. We note in passing that all of these will satisfy $\mu = z(\bar{L} + \varphi) = z(\bar{L} - \varphi)$ for their particular φ, and that we will have exactly one solution with phase φ in each of the regions $(0, \frac{\pi}{2}), (\frac{\pi}{2}, \pi), (\pi, \frac{3\pi}{2}), (\frac{3\pi}{2}, 2\pi)$.

Thus, as in the case where we had only $x \mapsto -x$ symmetry, we again see that the zero-level set of the function $Z(L, \varphi) := z(L + \varphi) - z(L - \varphi)$ describes all bifurcation branches of localized oscillatory structures. The $\mathcal{R}$-symmetric solution branches are those with $\varphi = 0$ and $\varphi = \pi$, while the $\kappa\mathcal{R}$ branches correspond to $\varphi = \frac{\pi}{2}$ and $\varphi = \frac{3\pi}{2}$. Both these solution types exist for all values of L. Finally, asymmetric solutions exist only for those values of L and $\varphi \notin \{0, \frac{\pi}{2}, \pi, \frac{3\pi}{2}\}$ such that $Z(L, \varphi) = 0$. See Figure 1 for the bifurcation diagram when z has the shape outlined in Figure 7(i).

Similar to the case without symmetry, these results have been derived rigorously in [3]: if a $\mathbb{Z}_2$ symmetry κ is present, the function z will be π rather than 2π-periodic, and two additional snaking branches with $\kappa\mathcal{R}$ symmetry will exist for $\mu = \mu_*(L, \varphi_0) = z(L + \varphi_0) + \mathrm{O}(e^{-KL})$ for some $K > 0$ with $\varphi_0 \in \{\frac{\pi}{2}, \frac{3\pi}{2}\}$.

2.7 Breaking $\mathbb{Z}_2$ symmetry or variational structure

We now preview the effects of adding a general reversible perturbation, which we will expand upon in the next two sections. Figure 10 provides an overview of these effects at the highest level.

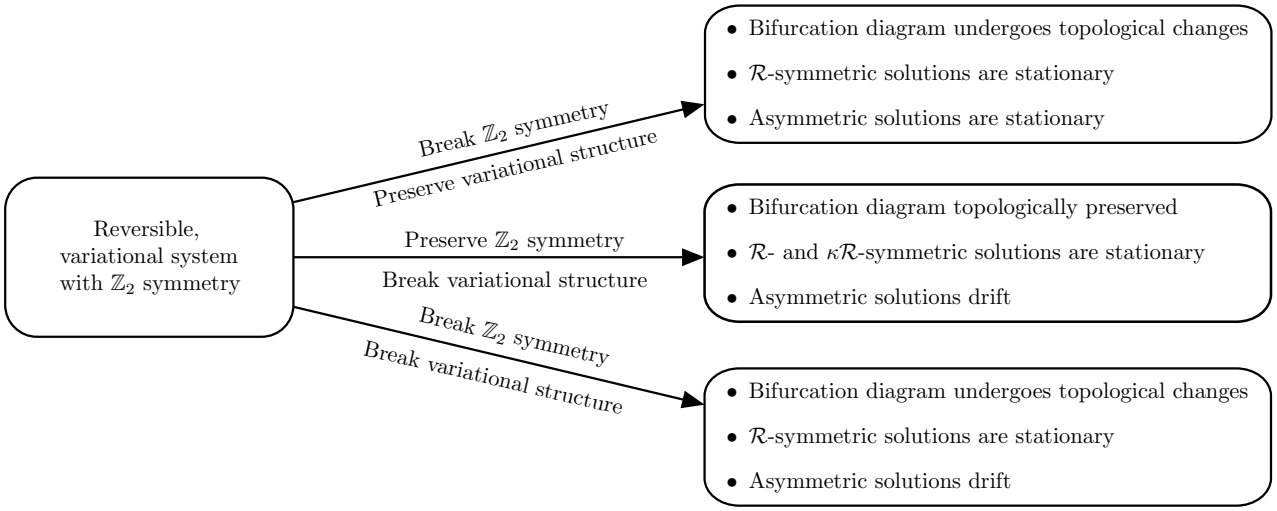

Figure 10: *A high-level summary of the effects of breaking $\mathbb{Z}_2$ symmetry, variational structure, or both. Perturbations breaking reversibility can also be overlaid on each of these, and are discussed in Section 4.3.*

First, those parts of the perturbation that break the $\mathbb{Z}_2$ symmetry will generically cause qualitative (topological) changes to the bifurcation diagram and underlying solution profiles, as they will induce changes in the function z and, in particular, break its π-periodicity. The new form of the bifurcation diagram can be determined by solving

$$Z(L, \varphi, \varepsilon) = z(L + \varphi, \varepsilon) - z(L - \varphi, \varepsilon) = 0, \tag{2.4}$$

where $z(\varphi, \varepsilon)$ is the ε-dependent z function. We discuss this further in Section 3.

Second, the nonvariational parts of the perturbation may cause localized patterns to drift: the existence of perturbed profiles and shape of the bifurcation branches is determined by (2.4); however, unless the perturbation also breaks the reversibility or $\mathbb{Z}_2$ symmetry, we do not expect qualitative differences in the solution profiles or branch shapes. On the other hand, these perturbed solutions may travel with nonzero speed, and Lemma 4.1 below predicts their speed to be

$$c = -\frac{1}{||u_x||_{L^2}^2} \langle u_x, G(u) \rangle_{L^2}$$

along a perturbed profile u.

3 Predicting the results of breaking $\mathbb{Z}_2$ symmetry

3.1 Dynamical reformulation of the problem

Our goal now is to start with a system that respects the $\mathbb{Z}_2$ symmetry κ for all μ, and to describe what happens under forced symmetry breaking. To illustrate our approach, we start with the case where $z(L)$ possesses one maximum and one minimum for each period π, where the π-periodicity is enforced by the presence of a $\mathbb{Z}_2$ symmetry κ. We will be interested in perturbative terms breaking the κ symmetry when a second parameter ε is switched on, i.e., when $\varepsilon \neq 0$.

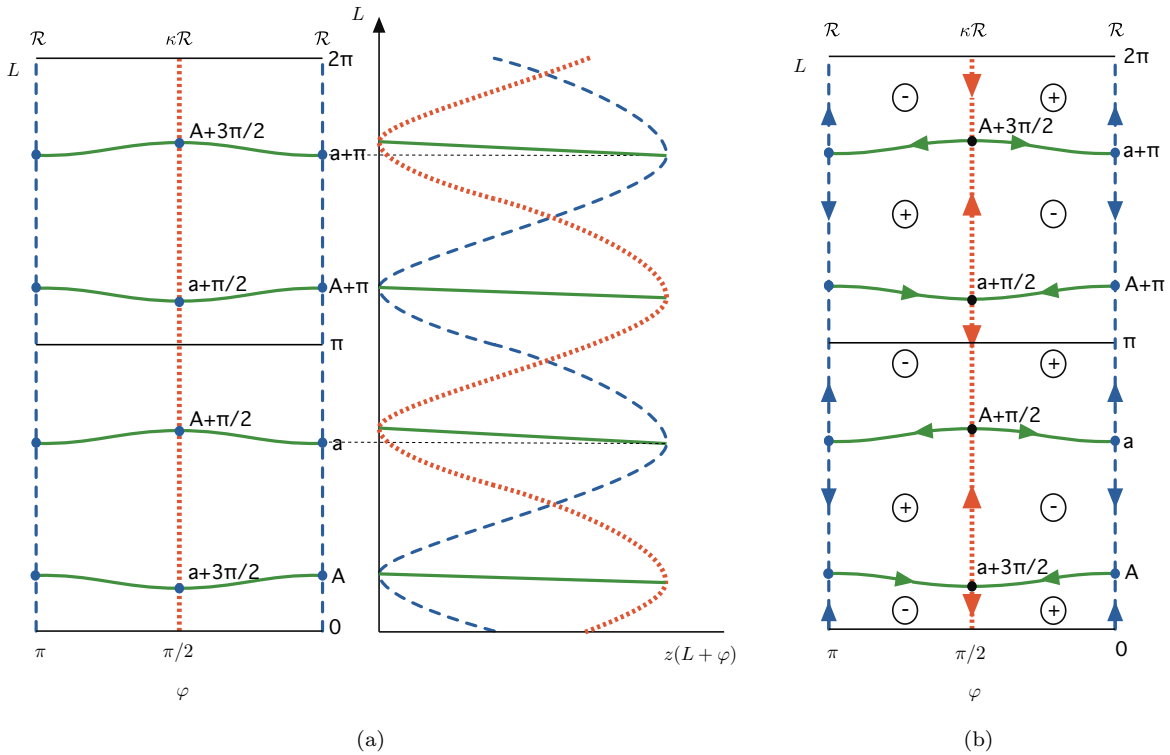

Figure 11: *We show different renderings of the bifurcation diagram for a system characterized by z possessing exactly one maximum and one minimum per period.* Left: *The solution set of the bifurcation equations $z(L-\varphi) = z(L+\varphi)$ is shown in the (φ, L)-plane.* Center: *The bifurcation diagram in the (μ, L)-plane, using the relation $\mu = z(L+\varphi)$. $\mathcal{R}$-symmetric solution branches with $\varphi = 0, \pi$ are shown in dashed blue, $\kappa\mathcal{R}$-symmetric with $\varphi = \frac{\pi}{2}, \frac{3\pi}{2}$ in dotted orange, and asymmetric in solid green. Light dotted lines indicate correspondence of a and $a+\pi$ with minima.* Right: *Reformulation of the left panel as a Hamiltonian system; see the text for full details.*

In Figure 11(a) we provide two equivalent renderings of the solution branches of localized structures in a system possessing κ symmetry and with $z(L)$ having a single maximum per period. We illustrate the branches of even and odd symmetric structures ($\mathcal{R}$- and $\kappa\mathcal{R}$-symmetric, respectively) as well as the asymmetric solution branches. The left panel shows the phase φ along the x-axis, and the half-pulse length L along the y-axis, while the center panel shows the solutions in the (μ, L) plane via the function $\mu = z(L+\varphi)$ for solutions (L, φ) of

$$Z(L, \varphi) := z(L+\varphi) - z(L-\varphi) = 0.$$

This is analogous to our usual bifurcation diagram, with length L being equivalent to the L^2 norm. The formulation in the left panel will provide a natural way to understand the effects of symmetry breaking perturbations, while the center panel provides the link to familiar bifurcation diagrams. We see that, before perturbation, the $\mathcal{R}$-symmetric solutions at $\varphi = 0$ and $\varphi = \pi$ coincide in the (μ, L) plane, as do the $\kappa\mathcal{R}$-symmetric solutions at $\varphi = \frac{\pi}{2}$ and $\varphi = \frac{3\pi}{2}$ (latter not shown). We also note that, due to the π-periodicity of z, all information is actually contained in a single quadrant of the left panel, but we show the larger diagram here for easier comparison with the diagram after symmetry breaking.

We now drop the assumption that z has only one maximum per period. We argued formally in Section 2 that it suffices to solve

$$Z(L, \varphi) := z(L+\varphi) - z(L-\varphi) = 0 \tag{3.1}$$

for (L, φ) in order to find symmetric and asymmetric solution branches. Indeed, it was shown in [3] that the bifurcation equations for symmetric and asymmetric solutions are given by (3.1) with an additional error term

of order $O(e^{-KL})$ for some $K > 0$: in particular, regular zeros of (3.1) persist as solutions to the full bifurcation equations for all sufficiently large L. The analysis in [3] applies to reversible PDEs with or without variational structure on cylinders provided the spatial dynamical system associated with the steady-state equation falls under the class considered in [18].

Our goal here is to study the effect of perturbative terms breaking the κ symmetry. It will be useful to consider the system presented in the left panel of Figure 11(a) as a dynamical system in its own right, a technique employed in [3]. We let $\bar{S}^1 := [0, \pi]/\sim$, set $Q := \bar{S}^1 \times [0, \frac{\pi}{2}]$, and define

$$\Lambda := \{(L, \varphi) \in Q : Z(L, \varphi) = 0\}, \quad \Lambda_{bif} := \{(L, \varphi) \in \partial Q : z'(L + \varphi) = 0\}.$$

We introduce the planar Hamiltonian vector field

$$\begin{pmatrix} L_s \\ \varphi_s \end{pmatrix} = F(L, \varphi) := \begin{pmatrix} 0 & 1 \\ -1 & 0 \end{pmatrix} \nabla Z(L, \varphi) \tag{3.2}$$

whose zero energy level is precisely equal to the set Λ. We note that

$$\nabla Z(L, \varphi) = \begin{pmatrix} 1 & -1 \\ 1 & 1 \end{pmatrix} \begin{pmatrix} z'(L + \varphi) \\ z'(L - \varphi) \end{pmatrix}.$$

Hence we have $\nabla Z(L, \varphi) = 0$ if and only if $z'(L + \varphi) = z'(L - \varphi) = 0$. Assuming nondegeneracy of the maxima and minima of z, i.e., assuming $z(L_1) = z(L_2)$ and $z'(L_1) = z'(L_2) = 0$ imply $L_1 = L_2 \bmod \pi$, we conclude that $\nabla Z(L, \varphi) = 0$ for $(L, \varphi) \in \Lambda$ if and only if $\varphi \in \{0, \frac{\pi}{2}\}$. Thus all equilibria of (3.2) in Λ lie in Λ_{bif}. Furthermore, assuming $z'(L) = 0$ implies $z''(L) \neq 0$, all equilibria in Λ are hyperbolic saddles, since at these points we have

$$DF(L, \varphi_0) = 2 \begin{pmatrix} z''(L + \varphi_0) & 0 \\ 0 & -z''(L + \varphi_0) \end{pmatrix}, \quad \varphi_0 \in \left\{0, \frac{\pi}{2}\right\}.$$

So by Poincaré–Bendixson, $\Lambda \backslash \Lambda_{bif}$ must be a 1D manifold consisting of the heteroclinic orbits that start and end at Λ_{bif}, and finitely many periodic orbits. Thus each element $(L_*, 0)$ and $(L_*, \frac{\pi}{2})$ of Λ_{bif} is a generic pitchfork bifurcation point, which gives rise to a unique global branch of solutions of (3.1) in Q. These branches do not cross, and they begin and end in Λ_{bif}. In Figure 11(b) we reproduce the left panel of Figure 11(a) with arrows indicating the flow of (3.2) within the zero energy level set Λ of the Hamiltonian system just described, as well as plus and minus signs indicating the sign of the energy $Z(L, \varphi)$.

We are now ready to consider a perturbation which breaks the κ symmetry, but preserves the other characteristics of our system, meaning in particular that the reversibility is unaffected so that we retain the 2π-periodicity of z. Such a symmetry breaking perturbation will, however, typically break the π-periodicity of z and therefore break up the $\kappa\mathcal{R}$-symmetric branch. On the level of the vector field interpretation, this manifests itself as the fact that the saddle equilibria persist, but generically move outside the zero-level set of Z.

Lemma 3.1 *Suppose $z(L)$ is π-periodic, satisfying (a) $z(L_1) = z(L_2)$ and $z'(L_1) = z'(L_2)$ only if $L_1 = L_2$ mod π and (b) $z'(L) = 0$ implies $z''(L) \neq 0$. Let (L_0, φ_0) be a hyperbolic equilibrium of (3.2) satisfying (3.1). Assume $\tilde{z}(L, \varepsilon) := z(L) + \varepsilon z_1(L) + O(\varepsilon^2)$, with $\tilde{z}(L, \varepsilon)$, and therefore $z_1(L)$, 2π-periodic in L. Further define $\tilde{Z}(L, \varphi, \varepsilon) := \tilde{z}(L + \varphi, \varepsilon) - \tilde{z}(L - \varphi, \varepsilon)$, and consider*

$$\begin{pmatrix} L_s \\ \varphi_s \end{pmatrix} = \tilde{F}(L, \varphi, \varepsilon) := \begin{pmatrix} 0 & 1 \\ -1 & 0 \end{pmatrix} \nabla \tilde{Z}(L, \varphi, \varepsilon). \tag{3.3}$$

Then there exists an $\varepsilon_0 > 0$ such that the following hold:

(i) If $\varphi_0 \in \{0, \pi\}$, then for all $|\varepsilon| < \varepsilon_0$ there exists a unique $\tilde{L}_0(\varepsilon)$ close to L_0 such that $(\tilde{L}_0(\varepsilon), \varphi_0, \varepsilon)$ is a hyperbolic equilibrium of (3.3), and $\tilde{Z}(\tilde{L}_0(\varepsilon), \varphi_0, \varepsilon) = 0$. Furthermore, the function $\varepsilon \mapsto \tilde{L}_0(\varepsilon)$ is smooth.

(ii) If $\varphi_0 \in \{\frac{\pi}{2}, \frac{3\pi}{2}\}$, then for all $|\varepsilon| < \varepsilon_0$ there exists a unique $(\tilde{L}_0, \tilde{\varphi}_0)(\varepsilon)$ close to (L_0, φ_0) such that $((\tilde{L}_0, \tilde{\varphi}_0)(\varepsilon), \varepsilon)$ is a hyperbolic equilibrium of (3.3). Furthermore, the function $\varepsilon \mapsto (\tilde{L}_0, \tilde{\varphi}_0)(\varepsilon)$ is smooth, and if $z_1(L_0 + \varphi_0) \neq z_1(L_0 - \varphi_0)$, then $\tilde{Z}((\tilde{L}_0, \tilde{\varphi}_0)(\varepsilon), \varepsilon) \neq 0$.

Proof. Given $\tilde{F}$ as defined in (3.3), we can write $\tilde{F}$ explicitly as

$$\tilde{F}(L, \varphi, \varepsilon) = \begin{pmatrix} \tilde{z}(L + \varphi, \varepsilon) + \tilde{z}(L - \varphi, \varepsilon) \\ -\tilde{z}(L + \varphi, \varepsilon) + \tilde{z}(L - \varphi, \varepsilon) \end{pmatrix} = \begin{pmatrix} z'(L + \varphi) + \varepsilon z_1'(L + \varphi) + z'(L - \varphi) + \varepsilon z_1'(L - \varphi) + \mathrm{O}(\varepsilon^2) \\ -z'(L + \varphi) - \varepsilon z_1'(L + \varphi) + z'(L - \varphi) + \varepsilon z_1'(L - \varphi) + \mathrm{O}(\varepsilon^2) \end{pmatrix}.$$

Whether we are in case (i) where $\varphi_0 \in \{0, \pi\}$, or case (ii) where $\varphi_0 \in \{\frac{\pi}{2}, \frac{3\pi}{2}\}$, the π-periodicity of z implies $z''(L_0 + \varphi_0) = z''(L_0 - \varphi_0)$ so that

$$D\tilde{F}(L_0, \varphi_0, 0) = \begin{pmatrix} 2z''(L + \varphi_0) & 0 & z_1'(L_0 + \varphi_0) + z_1'(L_0 - \varphi_0) \\ 0 & -2z''(L_0 + \varphi_0) & -z_1'(L_0 + \varphi_0) + z_1'(L_0 - \varphi_0) \end{pmatrix}. \tag{3.4}$$

Since we have assumed $z''(L_0 + \varphi_0) \neq 0$, this implies that there exists a $\varepsilon_0 > 0$ such that for all $|\varepsilon| < \varepsilon_0$, there exists a unique $(\tilde{L}_0, \tilde{\varphi}_0)(\varepsilon)$ close to (L_0, φ_0) such that $((\tilde{L}_0, \tilde{\varphi}_0)(\varepsilon), \varepsilon)$ is a hyperbolic equilibrium of (3.3), and the map $\varepsilon \mapsto (\tilde{L}_0, \tilde{\varphi}_0)(\varepsilon)$ is smooth.

In particular, we can solve for $(\tilde{L}_0, \tilde{\varphi}_0)(\varepsilon)$ as:

$$\tilde{F}(L, \varphi, \varepsilon) = \tilde{F}(L_0, \varphi_0, 0) + D\tilde{F}(L_0, \varphi_0, 0) \begin{pmatrix} L - L_0 \\ \varphi - \varphi_0 \\ \varepsilon \end{pmatrix} + \mathrm{O}(\varepsilon^2) = \begin{pmatrix} 0 \\ 0 \end{pmatrix}$$

so

$$\begin{pmatrix} 2z''(L_0 + \varphi_0)(L - L_0) + (z_1'(L_0 + \varphi_0) + z_1'(L_0 - \varphi_0))\varepsilon \\ -2z''(L_0 + \varphi_0)(\varphi - \varphi_0) + (-z_1'(L_0 + \varphi_0) + z_1'(L_0 - \varphi_0))\varepsilon \end{pmatrix} + \mathrm{O}(\varepsilon^2) = \begin{pmatrix} 0 \\ 0 \end{pmatrix}$$

yielding

$$L - L_0 = \varepsilon \left(\frac{-z_1'(L_0 + \varphi_0) - z_1'(L_0 - \varphi_0)}{2z''(L_0 + \varphi_0))} \right) + \mathrm{O}(\varepsilon^2)$$

$$\varphi - \varphi_0 = \varepsilon \left(\frac{-z_1'(L_0 + \varphi_0) + z_1'(L_0 - \varphi_0)}{2z''(L_0 + \varphi_0))} \right) + \mathrm{O}(\varepsilon^2)$$

or

$$(\tilde{L}_0, \tilde{\varphi}_0)(\varepsilon) = (L_0, \varphi_0) + \frac{\varepsilon}{2z''(L_0 + \varphi_0)} \left(-z_1'(L_0 + \varphi_0) - z_1'(L_0 - \varphi_0), -z_1'(L_0 + \varphi_0) + z_1'(L_0 - \varphi_0)\right) + \mathrm{O}(\varepsilon^2).$$

In case (i) where $\varphi_0 \in \{0, \pi\}$, the 2π-periodicity of $z_1(L)$ yields

$$(\tilde{L}_0, \tilde{\varphi}_0)(\varepsilon) = (L_0, \varphi_0) + \frac{\varepsilon}{2z''(L_0 + \varphi_0)} \left(-2z_1'(L_0 + \varphi_0), 0\right) + \mathrm{O}(\varepsilon^2).$$

In fact, for $\varphi_0 \in \{0, \pi\}$, the 2π-periodicity of $\tilde{z}(L, \varepsilon)$ in L implies that

$$\tilde{F}(L, \varphi_0, \varepsilon) = 2 \begin{pmatrix} \tilde{z}'(L + \varphi_0) \\ 0 \end{pmatrix}.$$

So the unique $(\tilde{L}_0, \tilde{\varphi}_0)(\varepsilon)$ near (L_0, φ_0) satisfying $\tilde{F}((\tilde{L}_0, \tilde{\varphi}_0)(\varepsilon), \varepsilon) = 0$ must be of the form $(\tilde{L}_0(\varepsilon), \varphi_0)$ where $\tilde{L}_0(\varepsilon)$ satisfies $z'(\tilde{L}_0(\varepsilon) + \varphi_0) + \varepsilon z_1'(\tilde{L}_0(\varepsilon) + \varphi_0) = 0$.

This then implies

$$\tilde{Z}(\tilde{L}_0(\varepsilon), \varphi_0, \varepsilon) = z(\tilde{L}_0(\varepsilon) + \varphi_0) + \varepsilon z_1(\tilde{L}_0(\varepsilon) + \varphi_0) - z(\tilde{L}_0(\varepsilon) - \varphi_0) + \varepsilon z_1(\tilde{L}_0(\varepsilon) - \varphi_0) = 0$$

as $\tilde{z}$ is 2π-periodic. Thus we have shown (i).

In case (ii) where $\varphi_0 \in \{\frac{\pi}{2}, \frac{3\pi}{2}\}$ we have

$$\tilde{Z}((\tilde{L}_0, \tilde{\varphi_0})(\varepsilon), \varepsilon) = z\left(L_0 + \varphi_0 - \frac{\varepsilon z_1'(L_0+\varphi_0)}{z''(L_0+\varphi_0)}\right) + \varepsilon z_1\left(L_0 + \varphi_0 - \frac{\varepsilon z_1'(L_0+\varphi_0)}{z''(L_0+\varphi_0)}\right) - z\left(L_0 - \varphi_0 - \frac{\varepsilon z_1'(L_0-\varphi_0)}{z''(L_0+\varphi_0)}\right) - \varepsilon z_1\left(L_0 - \varphi_0 - \frac{\varepsilon z_1'(L_0-\varphi_0)}{z''(L_0+\varphi_0)}\right) + \mathrm{O}(\varepsilon^2). \quad (3.5)$$

We expand

$$z\left(L_0 + \varphi_0 - \frac{\varepsilon z_1'(L_0+\varphi_0)}{z''(L_0+\varphi_0)}\right) = z(L_0+\varphi_0) + 2z'(L_0+\varphi_0)\left(\frac{-\varepsilon z_1'(L_0+\varphi_0)}{z''(L_0+\varphi_0)}\right) + \mathrm{O}(\varepsilon^2)$$

and similarly for $z\left(L_0 - \varphi_0 - \frac{\varepsilon z_1'(L_0-\varphi_0)}{z''(L_0+\varphi_0)}\right)$.

We also recall that $z'(L_0+\varphi_0) = z'(L_0-\varphi_0) = 0$, and $z(L_0+\varphi_0) - z(L_0-\varphi_0) = 0$. Thus we rewrite (3.5) as

$$\tilde{Z}((\tilde{L}_0, \tilde{\varphi_0})(\varepsilon), \varepsilon) = \varepsilon z_1(L_0+\varphi_0) - \varepsilon z_1(L_0-\varphi_0) + \mathrm{O}(\varepsilon^2)$$

so that $\tilde{Z}((\tilde{L}_0, \tilde{\varphi_0})(\varepsilon), \varepsilon) \neq 0$ as long as $z_1(L_0+\varphi_0) \neq z_1(L_0-\varphi_0)$. This completes the proof of (ii). ∎

The key point of the above is that saddle equilibria corresponding to pitchfork bifurcations from the $\kappa\mathcal{R}$-symmetric branches generically do not remain in the zero-level set of Z once the κ symmetry is broken, so that the $\kappa\mathcal{R}$-symmetric branches are themselves broken in a manner consistent with the Hamiltonian vector field formulation described above.

3.2 Implications for particular forms of z

3.2.1 Systems such that z has a single maximum per period

Returning to the case where z has only one maximum and minimum per period, in Figure 12 we illustrate one possible result of κ symmetry breaking in such a system. In particular, using notation from the figure and Lemma 3.1, we have illustrated the case where $z_1(A) > z_1(A+\pi)$ and $z_1(a) > z_1(a+\pi)$. This means that the saddle equilibrium near $(\frac{\pi}{2}, A+\frac{\pi}{2})$ will now lie in the region where $\tilde{Z} < 0$, since

$$z_1\left(\left(A+\frac{\pi}{2}\right)+\frac{\pi}{2}\right) = z_1(A+\pi) < z_1(A) = z_1\left(\left(A+\frac{\pi}{2}\right)-\frac{\pi}{2}\right).$$

Similarly, the equilibrium near $(a-\frac{\pi}{2}, \frac{\pi}{2})$ will lie in the region where $\tilde{Z} > 0$, since

$$z_1\left(\left(a-\frac{\pi}{2}\right)+\frac{\pi}{2}\right) = z_1(a) > z_1(a+\pi) = z_1(a-\pi) = z_1\left(\left(a-\frac{\pi}{2}\right)-\frac{\pi}{2}\right).$$

Note that the 2π-periodicity of z_1 implies that the sign of $\tilde{Z}$ for the saddle equilibria with $L \in [0, \pi)$ fixes the sign of $\tilde{Z}$ for the saddle equilibria with $L \in [\pi, 2\pi)$; specifically, the sign will be opposite.

Technically there are four possible generic bifurcation diagrams, one for each of the four possible combinations of the sign of $\tilde{Z}$ at saddle equilibria near $(\frac{\pi}{2}, A+\frac{\pi}{2})$ and $(\frac{\pi}{2}, a-\frac{\pi}{2})$. However, as is clear from the preceding discussion, the sign combinations $(+,+)$ and $(-,-)$ are equivalent under translation by π in L, which amounts to swapping our definition of the $\varphi = 0$ and $\varphi = \pi$ branches. This equivalence also holds for the sign combinations $(+,-)$ and $(-,+)$. Furthermore, these two sets of "same sign" and "opposite sign" bifurcation diagrams are in fact qualitatively equivalent as both result in a series of alternating cross-connecting and self-connecting asymmetric branches, each with two saddle nodes. In terms of the familiar bifurcation diagram in the (μ, L) plane, self-connecting branches will appear as 'S' shaped curves and cross-connecting as 'Z' shaped curves for

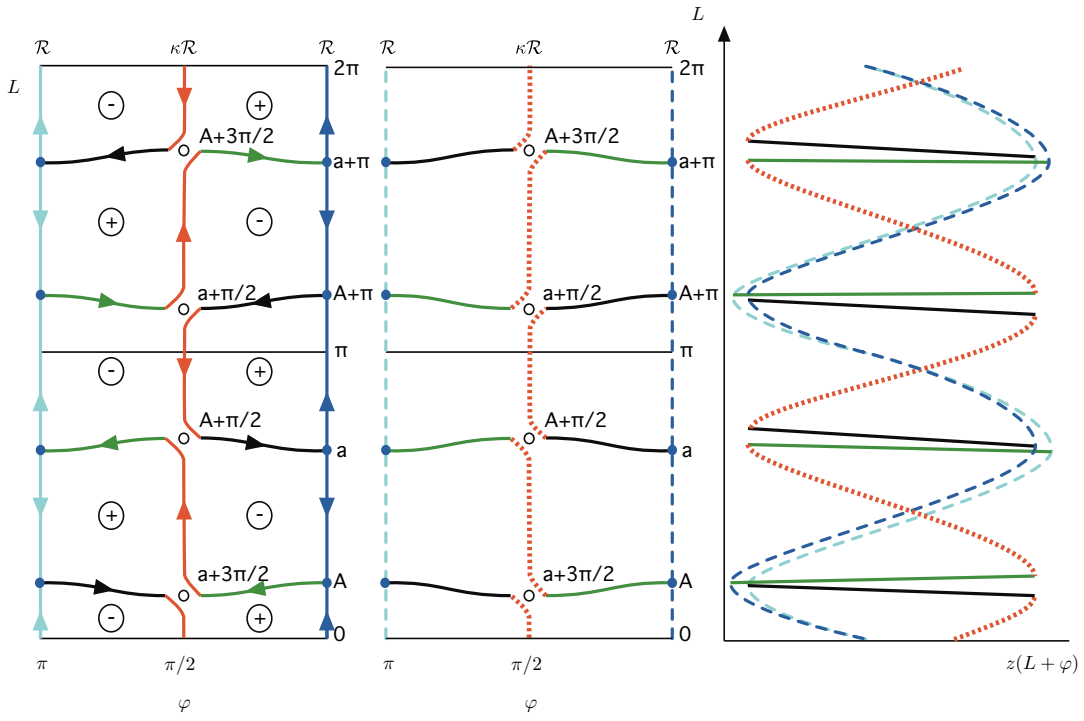

Figure 12: *Bifurcation diagram for a system as in Figure 11(a) after κ symmetry breaking. On the left is the interpretation of the branches as zero energy solutions of a Hamiltonian system, as in Figure 11(b); in the center is the same diagram without the vector field interpretation; and on the right the branches are shown in the $(\mu = z(L+\varphi), L)$ plane. The $\mathcal{R}$-symmetric branches, now appearing as two branches in the right-hand figure are shown in dashed dark and light blue for $\varphi = 0$ and π, respectively. The remains of the $\kappa\mathcal{R}$ symmetric branch, which now form sections of asymmetric branches, are shown in dotted orange. The portions of the asymmetric solution branches that were already asymmetric branches in the unperturbed case are shown in solid green and solid black to facilitate comparison of the diagrams.*

perturbations such that the sign of $\tilde{Z}$ is the same $[(+,+)$ or $(-,-)]$ for saddle equilibria with $L \in [0,\pi)$ near $\varphi = \pi/2$. The opposite is true for perturbations such that the sign of $\tilde{Z}$ is $(+,-)$ or $(-,+)$. As we will see below, when z has two or more maxima, different symmetry breaking perturbations may result in distinct bifurcation diagrams, which are not reducible via reflections or translations.

We note that these results are applicable to localized roll solutions of the one-dimensional Swift–Hohenberg model

$$u_t = -(1+\partial_x^2)^2 u - \mu u + \nu u^3 - u^5, \quad x \in \mathbb{R} \tag{3.6}$$

with the addition of perturbative terms, regardless of whether these terms preserve the variational structure. Indeed, we observe that these findings are entirely consistent with the numerical results of Houghton and Knobloch, including the breaking up of the odd parity branches, broadening of the snaking region, and appearance of S and Z asymmetric branches.

3.2.2 Systems such that z has at least two maxima per period

We now turn to the somewhat more complicated situation where $z(L)$ possesses two maxima and minima per period π; of course the periodicity implies that maxima and minima must occur in pairs.

Figure 13 shows a rendering of the resulting bifurcation structure for such a z. Again the left and center panels show the phase φ along the x-axis the pulse length L along the y-axis, while the right-hand figure shows the

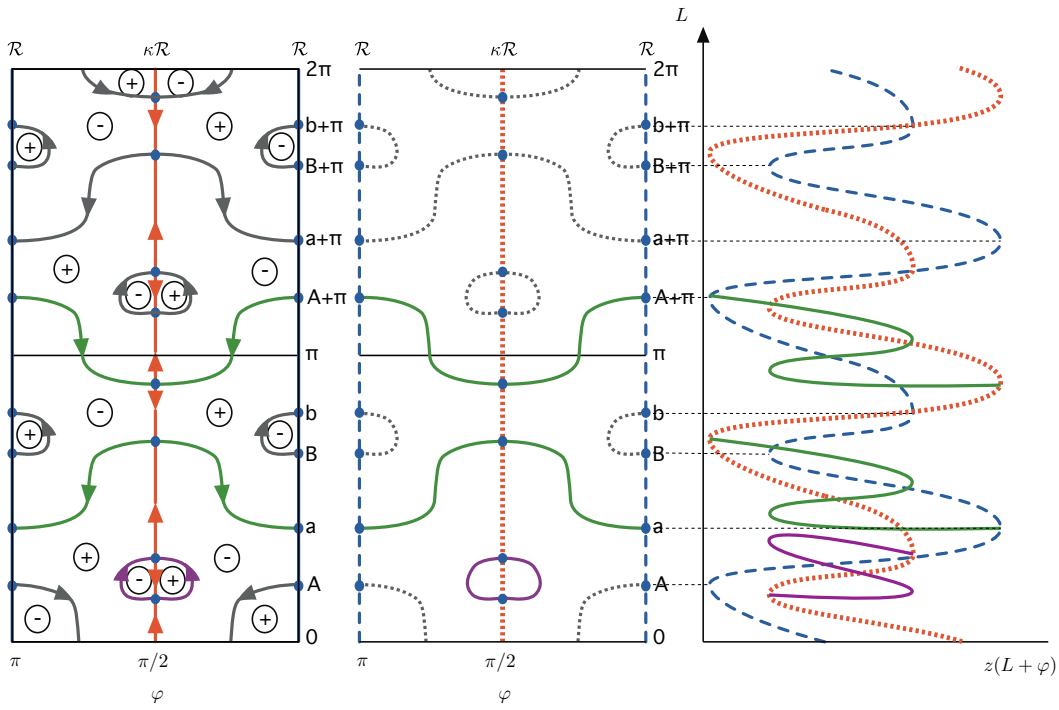

Figure 13: *Bifurcation structure of a system characterized by π-periodic z possessing two distinct maxima per period. Again, we illustrate the solution branches in the (φ, L) plane, both with and without the vector field interpretation, as well as in the $(\mu = z(L+\varphi), L)$ plane, where the actual bifurcation branches will be exponentially close in L to the ones shown. As before, $\mathcal{R}$-symmetric solution branches are shown in dashed blue, and $\kappa\mathcal{R}$-symmetric in dotted orange. Particular asymmetric solution branches are shown in solid purple and green. For clarity, not all asymmetric solution branches are shown in the right-most rendering; branches not shown on the right are rendered in thin dotted gray in the center illustration. The light dashed horizontal lines show the correspondence between the hyperbolic equilibria at A, a, B, b, etc. and the maxima and minima on the right.*

analogous plot to a typical bifurcation diagram. Once more, prior to perturbation, the $\mathcal{R}$-symmetric solutions at 0 and π coincide in the $(\mu = z(L+\varphi), L)$ plane, as do the $\kappa\mathcal{R}$-symmetric solutions at $\frac{\pi}{2}$ and $\frac{3\pi}{2}$. Again to enable later comparisons, we show the right and center diagrams for $(\varphi, L) \in [0, \pi] \times [0, 2\pi]$ even though all information is contained in the $[0, \frac{\pi}{2}] \times [0, \pi]$ quadrant.

We note that this form of z is observed for the planar stripe and spot patterns seen in the cubic-quintic Swift–Hohenberg posed on a cylinder, i.e.,

$$u_t = -(1 + \partial_x^2 + \partial_y^2)^2 u - \mu u + \nu u^3 - u^5, \quad (x, y) \in S^1 \times \mathbb{R} \tag{3.7}$$

where $S^1 = \mathbb{R}/2L_x\mathbb{Z}$ for some $L_x > 0$, and that the branches in Figure 13 are indeed consistent with the full bifurcation structure of the almost-planar stripe and spot patterns in the cubic-quintic Swift–Hohenberg model, as reported in [2] and also verified in Section 5 below.

Upon introduction of a perturbative term breaking the κ symmetry, we again expect that the $\kappa\mathcal{R}$-symmetric branches will break up, with the saddle equilibria generically moving outside the zero-level set of $\tilde{Z}$ due to the loss of π-periodicity of z, i.e., due to the fact that generically $z_1(L_0 + \varphi_0) \neq z_1(L_0 - \varphi_0)$. However, in contrast to the single maximum system discussed above, here we find that we obtain qualitatively different bifurcation diagrams depending on whether the new sign of $\tilde{Z}$ at adjacent saddle equilibria matches or differs.

In particular, there are now sixteen possible generic bifurcation diagrams, one for each of the possible combinations for the sign of $\tilde{Z}$ at saddle equilibria near $(\frac{\pi}{2}, B - \frac{\pi}{2})$, $(\frac{\pi}{2}, b - \frac{\pi}{2})$, $(\frac{\pi}{2}, A + \frac{\pi}{2})$ and $(\frac{\pi}{2}, a + \frac{\pi}{2})$, where the labels correspond to those used in Figure 13. Once again the 2π-periodicity of z_1 implies that the saddle equilibria

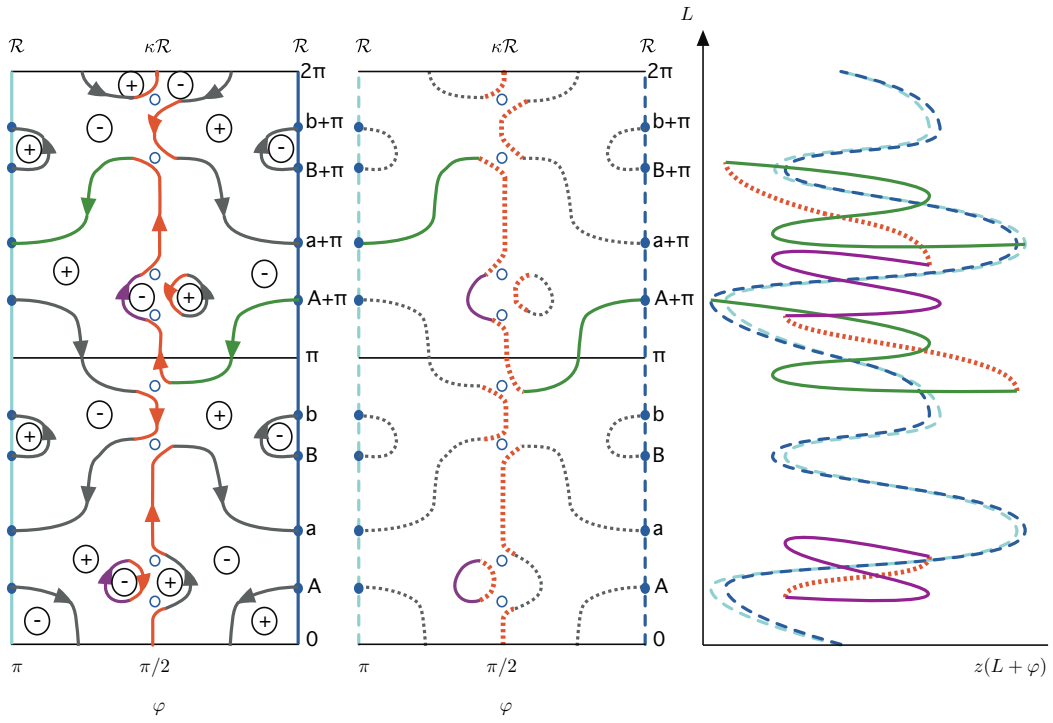

Figure 14: *Bifurcation structure of the system illustrated in Figure 13, after the addition of a κ symmetry breaking perturbative term causing the sign of Z to be the same at adjacent local extrema. Again for clarity, only a selection of asymmetric solution branches are shown in the right-most figure. The coloring and line styles from Figure 13 have been preserved to show the portions of each solution branch arising from the original branches in the unperturbed case. Note that although all branch segments bifurcating from the $\kappa\mathcal{R}$-symmetric branch remain dotted orange in the center figure, not all segments are shown on the right.*

with $L \in [\pi, 2\pi)$ will have $\tilde{Z}$ of the opposite sign as the corresponding saddle equilibria with $L \in [0, \pi)$.

Noting that B and b are local (rather than global) extrema of the function z, the biggest qualitative difference in possible bifurcation diagrams is between those in which the saddle equilibria near $(\frac{\pi}{2}, B - \frac{\pi}{2})$ and $(\frac{\pi}{2}, b - \frac{\pi}{2})$ have $\tilde{Z}$ with the same sign, versus those in which the sign of $\tilde{Z}$ is different. In the former case, the bifurcation diagram for the perturbed system will possess isolas formed from the reorganization of asymmetric and $\kappa\mathcal{R}$-symmetric branches, whereas in the latter the bifurcation diagram will have self-connecting asymmetric branches with many saddle nodes, but no isolas.

This distinction holds regardless of the sign of $\tilde{Z}$ at the remaining saddle equilibria, i.e., those corresponding to global maxima and minima. Differences in the sign of $\tilde{Z}$ for the saddle equilibria near $(\frac{\pi}{2}, A + \frac{\pi}{2})$ and $(\frac{\pi}{2}, a + \frac{\pi}{2})$ affect the number of saddle nodes in each asymmetric branch, but do not affect the formation of isolas. We note that, by inspection of the Hamiltonian vector field formulation, the exact number of saddle nodes on any given bifurcation branch can be determined by counting the number of tangencies to one of the vectors $(\pm 1, \pm 1)$ in the (φ, L) plane.

In Figure 14, we illustrate the form the bifurcation diagram should take under a perturbation such that z_1 at adjacent local extrema B and b satisfies $z_1(B) > z_1(B + \pi)$ and $z_1(b) > z_1(b + \pi)$. This means that the saddle equilibrium near $(\frac{\pi}{2}, B - \frac{\pi}{2})$ will now lie in the region where $\tilde{Z} > 0$, since

$$z_1\left(\left(B - \frac{\pi}{2}\right) + \frac{\pi}{2}\right) = z_1(B) > z_1(B + \pi) = z_1(B - \pi) = z_1\left(\left(B - \frac{\pi}{2}\right) - \frac{\pi}{2}\right).$$

The equilibrium near $(\frac{\pi}{2}, b - \frac{\pi}{2})$ will also lie in the region where $\tilde{Z} > 0$, since

$$z_1\left(\left(b - \frac{\pi}{2}\right) + \frac{\pi}{2}\right) = z_1(b) > z_1(b + \pi) = z_1(b - \pi) = z_1\left(\left(b - \frac{\pi}{2}\right) - \frac{\pi}{2}\right).$$

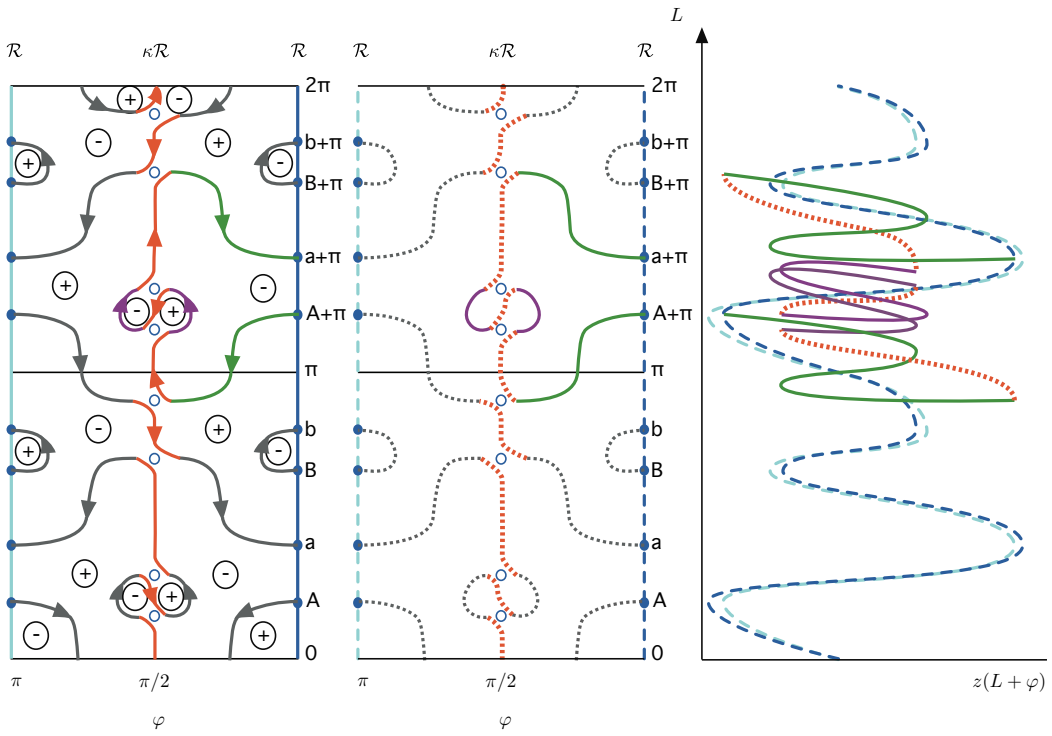

Figure 15: *Symmetry breaking with the opposite relative movement of adjacent local extrema from that displayed in Figure 14. Note that for clarity we no longer show a cross-connecting asymmetric solution, but focus instead on one of the self-connecting asymmetric branch with 14 saddle nodes.*

Again we observe that whether $z_1(B) > z_1(B+\pi)$ and $z_1(b) > z_1(b+\pi)$ or the opposite inequalities hold is immaterial as long as they are both in the same direction. Identifying these two cases amounts to reversing our conventions for defining $\varphi = 0$ and $\varphi = \pi$. In Section 5, we demonstrate the formation of isolas numerically for the Swift–Hohenberg model, with symmetry-breaking perturbation εu^2.

In contrast, in the case where the perturbation causes one local extremum to move up and the other to move down relative to those at distance π, we do not expect isolas, but rather anticipate a complicated asymmetric branch possessing 14 saddle nodes, as shown in Figure 15. In particular, we illustrate the case where $z_1(B) < z_1(B+\pi)$ and $z_1(b) > z_1(b+\pi)$, along with $z_1(A) > z_1(A+\pi)$ and $z_1(a) < z_1(a+\pi)$. As seen in Section 5, this type of behavior is observed in the Swift–Hohenberg model with the perturbative term εu^4.

This sort of analysis can be continued for z possessing more than two maxima per period. We reiterate that in order for symmetry breaking to produce isolas, a minimum of two maxima (and minima) are required prior to the introduction of symmetry breaking terms.

4 Full *a priori* characterization of perturbed bifurcation diagrams

We now derive conditions that allow us to predict bifurcation diagrams and drift speeds upon adding perturbative terms to the underlying system; these conditions rely on evaluation of the perturbative terms along solutions of the unperturbed system. We begin by examining the effects of breaking variational structure, then revisit perturbations breaking $\mathbb{Z}_2$ symmetry, and finally look at perturbations breaking reversibility.

4.1 Breaking variational structure

We begin by considering the drift speed c, which will generically be nonzero for the asymmetric branches of the perturbed system in the case where the perturbation $G(u)$ is nonvariational:

Lemma 4.1 *Assume that $u(x-ct)$ is a localized solution of $u_t = -\nabla\mathcal{E}(u) + G(u)$, where we assume that*

$$\mathcal{E}(u) = \int_{\mathbb{R}} \mathcal{L}(u(x), u_x(x), u_{xx}(x))dx$$

and

$$[G(u)](x) = g(u, u_x, u_{xx}, u_{xxx}). \tag{4.1}$$

Then $c = -\frac{1}{||u_x||_{L^2}^2}\langle u_x, G(u)\rangle_{L^2}$.

Proof. The function $u(x)$ satisfies $-\nabla\mathcal{E}(u) + cu_x + G(u) = 0$. Taking the scalar product with u_x we get

$$\begin{aligned} 0 &= -\int_{\mathbb{R}} \left(\mathcal{L}_u + \mathcal{L}_{u_x}\frac{\partial}{\partial x} + \mathcal{L}_{u_{xx}}\frac{\partial^2}{\partial x^2}\right) u_x dx + c||u_x||_{L^2}^2 + \int_{\mathbb{R}} u_x(x) g(u(x), u_x(x), u_{xx}(x), u_{xxx}(x))dx \\ &= -\int_{\mathbb{R}} \frac{d}{dx}\mathcal{L}(u(x), u_x(x), u_{xx}(x))dx + c||u_x||_{L^2}^2 + \int_{\mathbb{R}} u_x(x) g(u(x), u_x(x), u_{xx}(x), u_{xxx}(x))dx \\ &= c||u_x||_{L^2}^2 + \int_{\mathbb{R}} u_x(x) g(u(x), u_x(x), u_{xx}(x), u_{xxx}(x))dx, \end{aligned}$$

where we have used the fact that u is localized to conclude that $\int \frac{d}{dx}\mathcal{L}(u(x), u_x(x), u_{xx}(x)) = 0$. Hence, $c = -\frac{1}{||u_x||_{L^2}^2}\langle u_x, G(u)\rangle_{L^2}$. ∎

Thus, given a perturbation $\varepsilon G(u)$, the speed c^ε along a perturbed branch u^ε will be

$$c^\varepsilon = -\frac{1}{||u_x^\varepsilon||_{L^2}^2}\left\langle u_x^\varepsilon, \varepsilon G(u^\varepsilon)\right\rangle_{L^2}.$$

Evaluating this directly requires knowledge of the perturbed solution profiles. However, for ε small, we can predict the speeds of the perturbed solutions using only the original (unperturbed) solution profiles since

$$\left.\frac{dc}{d\varepsilon}\right|_{\varepsilon=0} = -\frac{1}{||u_x^0||_{L^2}^2}\left\langle u_x^0, G(u^0)\right\rangle_{L^2}, \tag{4.2}$$

where the right-hand side is computed for the unperturbed solutions. We now record a few consequences of this expression.

First, we reiterate that any solution which respects a reverser (either $\mathcal{R}$ or $\kappa\mathcal{R}$) must necessarily be stationary. However, as we will see explicitly in Section 5, once the reverser $\kappa\mathcal{R}$ is broken, a solution may be very close to respecting this (now nonexistent) reverser, and yet have a relatively large drift.

Second, we observe that drift speeds approach zero for reversible perturbations that break the variational structure as we proceed up the bifurcation diagram: if we decompose the inner products into contributions from the tails and the periodic orbits, we can write

$$||u_x^0||_{L^2}^2 \approx 2C_1 + N\int_0^{2\pi} u_x^0(x)^2 dx,$$

where N is the number of oscillations and C_1 arises from the integral over the tails and is independent of N; similarly

$$\left\langle u_x^0, G(u^0)\right\rangle_{L^2} \approx 2C_2 + N\int_0^{2\pi} u_x^0(x) g(u^0(x), u_x^0(x), u_{xx}^0(x), u_{xxx}^0(x))dx,$$

where again C_2 arises from the tails. Thus

$$\frac{dc}{d\varepsilon} \approx \frac{\int_0^{2\pi} u_x^0(x) g(u^0(x), u_x^0(x), u_{xx}^0(x), u_{xxx}^0(x)) dx}{\int_0^{2\pi} u_x^0(x)^2 dx} + \mathrm{O}\left(\frac{1}{N}\right).$$

However, along the wavetrains, $\int_0^{2\pi} u_x^0(x) g(u^0(x), u_x^0(x), u_{xx}^0(x), u_{xxx}^0(x)) dx$ will in fact be zero, as wave trains and the perturbation g are reversible, and we conclude that $dc/d\varepsilon$ indeed decays with rate at least $1/N$.

Finally, we remark that additional insight into the drift speed may be gained by approaching the problem via the spatial Hamiltonian, and verifying that we arrive at the same formula for the speed c. We do this for the one-dimensional Swift–Hohenberg equation, as we have an explicit expression for its Hamiltonian H. The main point we take away from the computation is that the speed is selected to guarantee spatial energy balance across the pattern. We start by writing

$$u_t = -(1+\partial_x^2)^2 u - \mu u + c u_x + \nu u^3 - u^5 + \varepsilon G(u).$$

We define $U = (U_0, U_1, U_2, U_3) = (u, u', u'', u''')$ so that the vector field is given by

$$U_x = F(U) + (c(U_1) + \varepsilon g(U_0, U_1, U_2, U_3)) \cdot (0\ 0\ 0\ 1)^\intercal$$

with

$$F(U) = \begin{pmatrix} 0 & 1 & 0 & 0 \\ 0 & 0 & 1 & 0 \\ 0 & 0 & 0 & 1 \\ -(1+\mu) & 0 & -2 & 0 \end{pmatrix} \begin{pmatrix} U_0 \\ U_1 \\ U_2 \\ U_3 \end{pmatrix} + \begin{pmatrix} 0 \\ 0 \\ 0 \\ \nu U_0^3 - U_0^5 \end{pmatrix}.$$

The spatial Hamiltonian is given by

$$H(U) = U_1 U_3 - \frac{U_2^2}{2} + U_1^2 + \frac{(1+\mu)U_0^2}{2} - \frac{\nu U_0^4}{4} + \frac{U_0^6}{6}.$$

In order to balance the Hamiltonian across a localized pattern $U(x)$, we should have

$$\begin{aligned}
0 &= H(U(+\infty)) - H(U(-\infty)) \\
&= \int_{\mathbb{R}} \frac{d}{dx} H(U(x)) dx \\
&= \int_{\mathbb{R}} \nabla H(U(x)) \cdot U_x(x) dx \\
&= \int_{\mathbb{R}} \nabla H(U(x)) \cdot (F(U(x)) + [c(U_1(x)) + \varepsilon g(U_0(x), U_1(x), U_2(x), U_3(x))] \cdot (0\ 0\ 0\ 1)^\intercal) dx \\
&= \int_{\mathbb{R}} \begin{pmatrix} (1+\mu)U_0(x) - \nu U_0(x)^3 + U_0(x)^5 \\ 2U_1(x) + U_3(x) \\ -U_2(x) \\ U_1(x) \end{pmatrix}^\intercal \times \\
&\quad \times \left(F(U(x)) + [c(U_1(x)) + \varepsilon g(U_0(x), U_1(x), U_2(x), U_3(x))] \cdot \begin{pmatrix} 0 \\ 0 \\ 0 \\ 1 \end{pmatrix} \right) dx \\
&= \varepsilon \int_{\mathbb{R}} U_1(x) g(U_0(x), U_1(x), U_2(x), U_3(x)) dx + c \int_{\mathbb{R}} U_1(x)^2 dx,
\end{aligned}$$

where we use the fact that $\nabla H(U(x)) \cdot F(U(x)) = 0$. Our final expression is, of course, the same expression we arrived at originally in Lemma 4.1. Thus we have the alternative interpretation that the speed is determined by the need to balance the spatial energy across the pattern.

4.2 Breaking $\mathbb{Z}_2$ symmetry

The analysis in Section 3 rigorously predicts the results of symmetry breaking and allows us to categorize all possible scenarios resulting from different forms of $\tilde{z}$. It does not, however, immediately provide a means to predict the particular reorganization resulting from a given perturbative term. In the following, we provide a method for predicting the full bifurcation diagram induced by a particular perturbation without the need for any computations on the perturbed system. For clarity we carry out our analysis for the Swift–Hohenberg model equation in one dimension, but it should be clear how to adapt this to more general settings.

We define

$$F(u,\mu,c,\varepsilon) := -(1+\partial_x^2)^2 u - \mu u + cu_x + bu^3 - u^5 + \varepsilon G(u) \tag{4.3}$$

where the perturbative term $G(u)$ is of the form given in (4.1), e.g., u^2 or u_x^2, and we have added the cu_x term to account for the fact that localized solutions may now drift so we may need to view them in a moving frame. We can then parameterize a solution branch for the unperturbed system as $(u^0(s),\mu^0(s))$, where s is, for instance, arc length along the branch, so that

$$F(u^0(s),\mu^0(s),0,0) = 0$$

for all s. We denote the tangent vector to this solution branch by

$$(u_s^0,\mu_s^0) := \frac{d}{ds}(u^0,\mu^0)(s).$$

For ε nonzero, the persisting $\mathcal{R}$-symmetric branch will be given by $(u^\varepsilon(s),\mu^\varepsilon(s),c^\varepsilon(s))$, which satisfies

$$F(u^\varepsilon(s),\mu^\varepsilon(s),c^\varepsilon(s),\varepsilon) = 0.$$

Differentiating this with respect to ε and evaluating at $\varepsilon = 0$, we obtain

$$F_u u_\varepsilon^0 + F_\mu \mu_\varepsilon^0 + F_c c_\varepsilon^0 + F_\varepsilon = 0, \tag{4.4}$$

where the derivatives of F are evaluated along (u^0,μ^0,c^0). Whether the perturbation $G(u)$ is variational or not, as shown in Lemma 3.1, the only information we need to complete the full bifurcation diagram of the perturbed system is local information on z_1 at $L_0+\varphi_0$ and $L_0-\varphi_0$. Thus we are only interested in what we will refer to as the "splitting distances," i.e., the difference between the values of μ at the saddle nodes of the unperturbed and perturbed $\mathcal{R}$-symmetric branches, which persist for any perturbation preserving the reverser $\mathcal{R}$. Consequently, we only require computations along the $\mathcal{R}$-symmetric branch, which continues to have $c = 0$ for $\varepsilon \neq 0$ as long as the reverser $\mathcal{R}$ persists. Defining $\mathcal{L} = -(1+\partial_x^2)^2 - \mu + 3bu^2 - 5u^4$ for a particular solution $(u,\mu) = (u^0,\mu^0)$, we see that

$$\begin{cases} \mathcal{L}u_\varepsilon^0 - u^0\mu_\varepsilon^0 + G(u^0) = 0 \\ \left\langle u_\varepsilon^0, u_s^0 \right\rangle_{L^2} + \mu_\varepsilon^0\mu_s^0 = 0. \end{cases} \tag{4.5}$$

Conversely, the system

$$\begin{cases} \mathcal{L}\tilde{u} - u^0\tilde{\mu} + G(u^0) = 0 \\ \left\langle \tilde{u}, \mu_s^0 \right\rangle_{L^2} + \tilde{\mu}\mu_s^0 = 0 \end{cases} \tag{4.6}$$

has generically a unique solution, which is therefore $(\tilde{u},\tilde{\mu}) = (u_\varepsilon^0,\mu_\varepsilon^0)$. Thus the offset along the solution branch will be given by $\mu_\varepsilon^0\varepsilon + \mathrm{O}(\varepsilon^2)$. We can find μ_ε^0 anywhere along the solution branch by solving the linear system (4.6).

Alternatively, we note that, at a saddle node, we have $\mu_s^0 = 0$ so that $\mathcal{L}u_s^0 = 0$; since $\mathcal{L}$ is self-adjoint in L^2, applying $\left\langle u_s^0, \cdot \right\rangle_{L^2}$ to the first equation in (4.5) yields

$$-\left\langle u_s^0, u^0\mu_\varepsilon^0 \right\rangle_{L^2} + \left\langle u_s^0, G(u^0) \right\rangle_{L^2} = 0$$

or

$$\mu_\varepsilon^0 = \frac{\langle u_s^0, G(u^0)\rangle_{L^2}}{\langle u_s^0, u^0\rangle_{L^2}}, \qquad \mathcal{L}u_s^0 = 0. \tag{4.7}$$

Thus we need only to calculate a solution (u^0, μ^0) and its associated eigenfunction u_s^0 to compute the offset at a saddle node. While the method of directly solving the linear system (4.6) is somewhat more robust numerically, the latter method given by (4.7) provides helpful insight, particularly in the one-dimensional case, and we refer to Section 5 for computations.

We emphasize that, whichever method we use, this calculation allows us to describe the full bifurcation diagram without the need for any computations on the perturbed system. The quantity μ_ε^0 corresponds to z_1 as defined in Lemma 3.1, which in turn determines which class of bifurcation diagram the perturbed system will exhibit. For example, in the case of a system with two left and two right saddle nodes per period π, we have seen that the formation of isolas depends on the relative signs of the difference in offsets for the inner saddle nodes at distance π. Indicating these nodes by $B, B+\pi, b, b+\pi$ as in Section 3.2.2, isolas will be formed if the quantity

$$\delta_{\mathbb{Z}_2} = (z_1(B) - z_1(B+\pi))(z_1(b) - z_1(b+\pi))$$

is greater than zero, but not if $\delta_{\mathbb{Z}_2}$ is less than zero.

Finally, while we know that for any perturbation $G(u)$ preserving $\mathbb{Z}_2$ symmetry, the function z_1 must remain π-periodic and therefore $\delta_{\mathbb{Z}_2}$ will be zero, it is instructive to understand heuristically why this quantity is zero for such a perturbation. Noting that the eigenfunctions are exponentially localized at the interfaces, and that at the interfaces solutions at distance π are related by κ symmetry, we see that for perturbations such that $G(\kappa u) = \kappa G(u)$, we will have $z_1(L) = z_1(L+\pi)$ for any L corresponding to a saddle node. Thus we will have $\delta_{\mathbb{Z}_2} = 0$ for a perturbation respecting κ symmetry so that the bifurcation diagram is topologically preserved.

4.3 Breaking reversibility

As mentioned in section 2, front solutions $u_f(x)$ and back solutions $u_b(x)$ in reversible systems are pairwise related via $u_b(x) = u_f(-x)$. In other words, the function $\mu = z(L)$ that connects interface length and parameter is the same for the front $u_f(x)$ and the back $u_b(x) = u_f(-x)$. This is no longer the case when perturbations of amplitude ε are added to the system that break the reversibility. Both fronts and backs will persist but they will, in general, no longer be related by reflection symmetry: in particular, the existence region of fronts and backs are described by functions $z_{f,b}(L,\varepsilon) = z(L) + \varepsilon w_{f,b}(L) + O(\varepsilon^2)$, respectively, where generally $w_f \not\equiv w_b$. We assume that $z(L)$ has precisely one minimum at $L = L_m$ and one maximum at $L = L_M$, both therefore corresponding to saddle-nodes in the unperturbed bifurcation diagram. As shown in [16, 22], there are two qualitatively different bifurcation diagrams for $\varepsilon \neq 0$ that depend on whether the quantity

$$\delta_{rev} = (w_f(L_M) - w_b(L_M))(w_f(L_m) - w_b(L_m))$$

is positive or negative. In both references, explicit perturbations, found by trial and error, were presented that yield either inequality. Here, we demonstrate that we can predict the sign of this quality a priori, using numerical computations of the unperturbed system only.

For the sake of clarity, we focus once more on the one-dimensional quadratic-cubic Swift–Hohenberg equation given by

$$u_t = -(1+\partial_x^2)^2 u - \mu u + bu^2 - u^3 + \varepsilon g(u, u_x, u_{xx}, u_{xxx}),$$

where we added a perturbation g that breaks the reversibility operation $x \mapsto -x$. We can now determine the offset $\mu' = d\mu/\varepsilon(0) = w_f(L_{M,m})$ as before separately at the left and right saddle-node bifurcations via

$$w_f(L_{M,m}) = \frac{\left\langle v_f, g(u_f(\cdot), u_f'(\cdot), u_f''(\cdot), u_f'''(\cdot))\right\rangle_{L^2}}{\langle v_f, u_f\rangle_{L^2}},$$

where u_f is the unperturbed front solution at the left or right saddle-node, while v_f is the associated eigenfunction of the linearization of the unperturbed Swift–Hohenberg equation at $\varepsilon = 0$. A similar expression holds for $w_b(L_{M,m})$. Noting that the unperturbed front u_f and back u_b as well as the eigenfunctions v_f and v_b are related by symmetry, it is easy to show that we have

$$w_f(L_{M,m}) - w_b(L_{M,m}) = \frac{\left\langle v_f, [g(u_f(\cdot), u_f'(\cdot), u_f''(\cdot), u_f'''(\cdot)) - g(u_f(\cdot), -u_f'(\cdot), u_f''(\cdot), -u_f'''(\cdot))] \right\rangle_{L^2}}{\langle v_f, u_f \rangle_{L^2}}, \tag{4.8}$$

again with the convention that u_f and v_f are calculated at the folds corresponding to $L = L_{M,m}$.

Equation (4.8) can now be evaluated by computing u_f and v_f numerically. Recall that symmetric localized patterns of length $2L$ arise by gluing a front and a back together. Hence, computing half of a localized pattern on a sufficiently large domain gives an accurate approximation of the front up to terms that are exponentially small in L.

5 Numerical confirmation of predictions

We now present several numerical studies supporting our analytical results. We examine perturbations breaking $\mathbb{Z}_2$ symmtetry, variational structure, and reversibility using the Swift–Hohenberg equations posed on both the line and the plane.

5.1 1D Swift–Hohenberg

In this section we illustrate how our analysis can be used to understand previously published work, and present new results. In Sections 5.1.1 and 5.1.2 we consider the family of equations

$$u_t = -(1 + \partial_x^2)^2 u - \mu u + \nu u^3 - u^5 + \varepsilon G(u) \tag{5.1}$$

posed on the real line, while in Section 5.1.3 we consider

$$u_t = -(1 + \partial_x^2)^2 u - \mu u + \nu u^2 - u^3 + \varepsilon G(u) \tag{5.2}$$

again posed on the real line, with a particular form for $G(u)$ introduced in [16].

5.1.1 Breaking $\mathbb{Z}_2$ symmetry

The bifurcation diagram for (5.1) with $G(u) = u^2$ was published in [15], and we have already seen how our analysis allows us to understand the form of the diagram. In addition to allowing us to predict the topological form of the bifurcation diagram given any perturbation, our approach has the added benefit of allowing us to understand particular features, such as the numerically observed unequal splitting on the left and right sides of snaking bifurcation diagrams, i.e., the fact that saddle nodes shift more on one side of the snaking diagram than on the other side upon introduction of symmetry breaking perturbative terms. Houghton and Knobloch noted this in their numerical study of symmetry-breaking in the one-dimensional cubic-quintic Swift–Hohenberg model, and we can see this in the numerically computed bifurcation diagrams shown in Figures 22(a) and 22(b) (or in Table 1) in Section 5.2, which exhibit greater displacement of the outer saddle nodes on the left compared to those on the right.

In Figure 16 we show four successive saddle nodes for the one-dimensional cubic-quintic Swift–Hohenberg equation prior to perturbation. We see that the solution $u(x)$ at successive left-hand saddle nodes is related by $u \mapsto -u$ symmetry, and similarly on the right. We also graph the saddle node eigenfunction $v(x)$ and the perturbative terms $u^2(x)$ and $u^4(x)$. Recalling that the offset will be determined by the ratio of the inner product

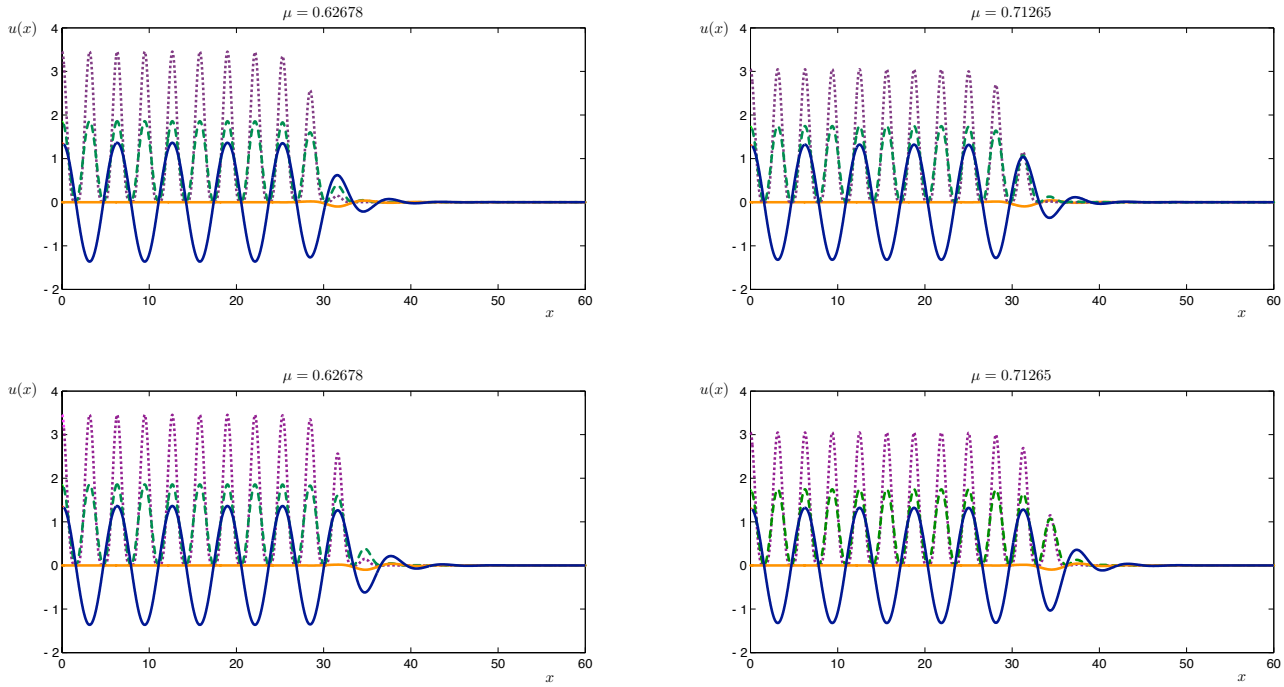

Figure 16: *Four successive saddle nodes, i.e., one full 2π-period along the snaking $\mathcal{R}$-symmetric branch, for the one-dimensional Swift–Hohenberg equation without perturbation. Solution $u(x)$ in solid blue, saddle node eigenfunction $v(x)$ in solid orange, $G(u) = u^2$ in dashed green and $G(u) = u^4$ in dotted purple.*

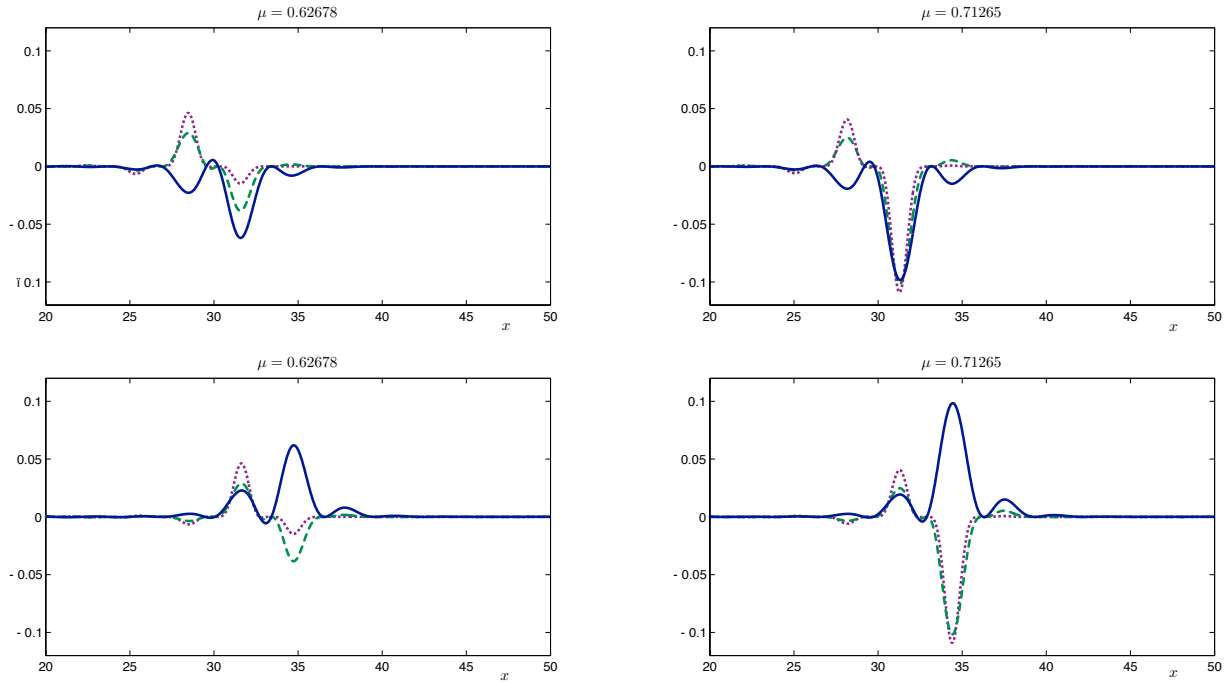

Figure 17: *The same four successive saddle nodes as in Figure 16, but now showing the pointwise product of the eigenfunction $v(x)$ with $u(x)$, $u^2(x)$, and $u^4(x)$. The function $(uv)(x)$ is shown in solid blue, $(u^2v)(x)$ in dashed green and $(u^4v)(x)$ in dotted purple.*

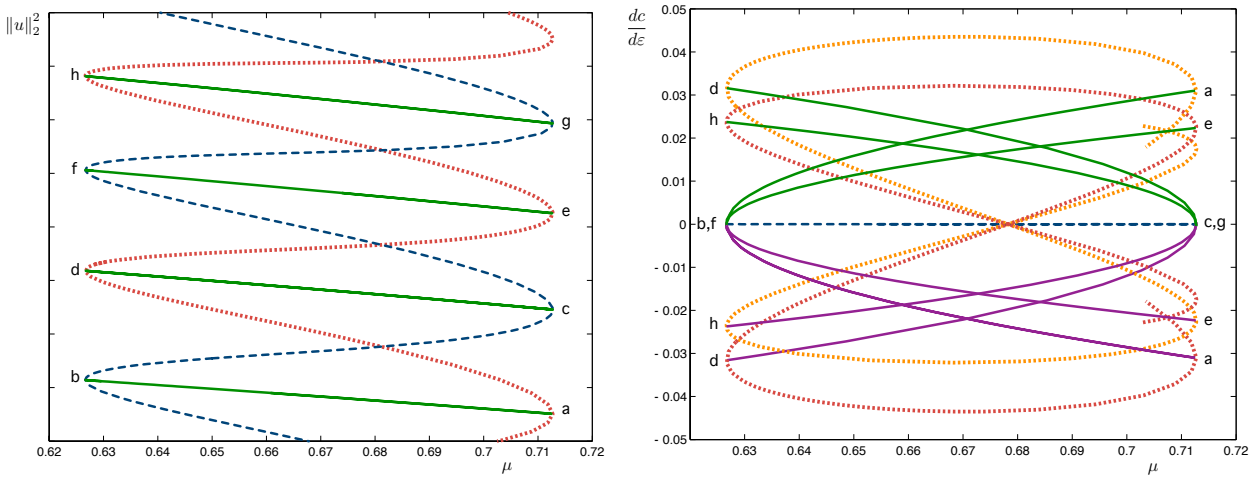

Figure 18: Left: *Bifurcation diagram for the one-dimensional cubic-quintic Swift–Hohenberg equation, with $\varepsilon = 0$; the $\mathcal{R}$-symmetric branch is shown in dashed blue, $\kappa\mathcal{R}$-symmetric branch in dotted orange, and four asymmetric branches in solid green. Saddle nodes are labeled (a) - (h) for comparison with right panel as well as left and right panels in Figure 19.* Right: $\frac{dc}{d\varepsilon}$ *for the perturbation $G(u) = u_x^2$, computed along the unperturbed branches shown at left: $\mathcal{R}$-symmetric in dashed blue at 0; $\kappa\mathcal{R}$-symmetric in dotted light and dark orange for the two profiles that drift in opposite directions; and asymmetric branches in solid green and purple for the two sets of two profiles that drift in opposite directions. Labels (a) - (h) correspond to the saddle nodes indicated at left.*

$\langle v, G(u)\rangle_{L^2}$ to $\langle v, u\rangle_{L^2}$, in Figure 17 we show the pointwise products of $v(x)$ with $u(x)$, $u^2(x)$, and $u^4(x)$. We observe that at the left saddle node, the peaks of $(u^2v)(x)$ and $(u^4v)(x)$ are approximately the same size, leading to a small value for $\langle v, G(u)\rangle_{L^2}$, which results in a smaller offset. On the other hand, for the saddle nodes on the right, u^2 and u^4 both exhibit a dominant peak, so that $\langle v, G(u)\rangle_{L^2}$ is of similar order to $\langle v, u\rangle_{L^2}$, resulting in a larger offset. The difference between the signs of the offsets for $G(u) = u^2$ and $G(u) = u^4$ is somewhat more subtle, though as we have noted already, in the one-dimensional case all offsets lead to qualitatively similar bifurcation diagrams.

5.1.2 Breaking variational structure

We next illustrate how our results can be used to understand the effects of the perturbation εu_x^2, which breaks both the $\mathbb{Z}_2$ symmetry and the variational structure of (5.1). The bifurcation diagram for this equation was also studied in [15].

In Figure 18 on the left we show a partial bifurcation diagram for (5.1), and on the right of Figure 18 we show the predicted values of $\frac{\partial c}{\partial \varepsilon}$ with the perturbative term $\varepsilon G(u) = \varepsilon u_x^2$ for the same set of branches. The latter are computed from the unperturbed solution profiles using (4.2). The $\mathcal{R}$-symmetric branch consisting of two solutions will not move: though the variational structure is broken, the reverser $\mathcal{R}$ remains upon introduction of ε. Conversely, the solutions along the $\kappa\mathcal{R}$-symmetric branch will begin to move since this reverser will no longer exist. We note that these observations are automatically encoded in the formula (4.2), and do not require any special enforcement. We also observe that the drift speeds are predicted to be largest low on the bifurcation diagram, and will decrease moving up along the bifurcation diagram, as noted in Section 4.1. With the exception of isolated solutions with zero predicted drift speed, we also further observe that at each point along the $\kappa\mathcal{R}$ symmetric-branch, one solution will begin to drift with positive speed and the other with equal and opposite speed (i.e., one will drift left and the other right.) This is actually particular to the perturbation: the solutions are related by $\kappa : u \mapsto -u$, and in this case $G(\kappa u) = G(u)$. This also explains the alternating positive and negative signs of the drift speeds along the $\kappa\mathcal{R}$ solution branch: the fronts at distance π (successive saddle nodes

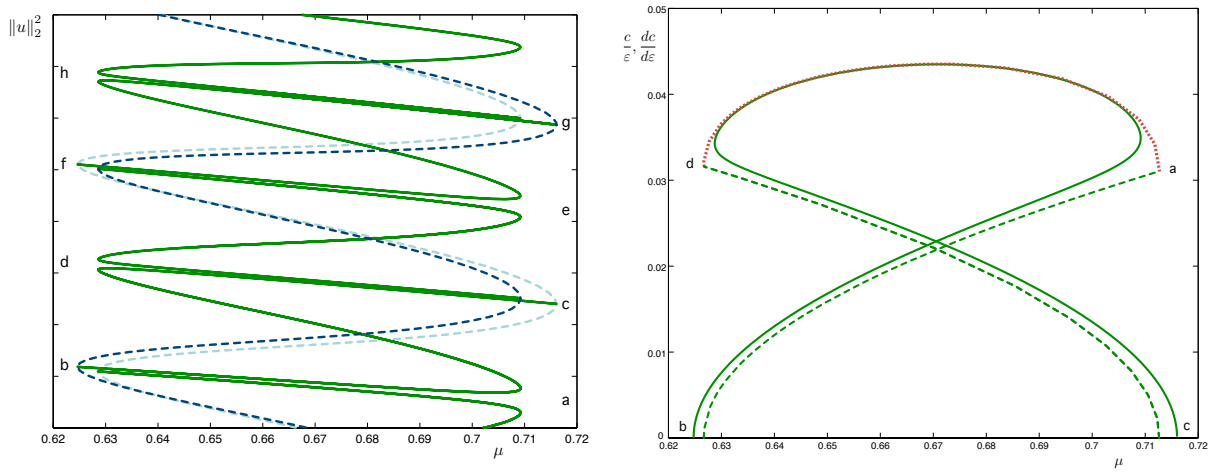

Figure 19: Left: *Bifurcation diagram for (5.1) with $G(u) = u_x^2$, and $\varepsilon = 0.01$. One $\mathcal{R}$-symmetric branch is shown in dashed dark blue, and the other $\mathcal{R}$-symmetric branch is shown in dashed light blue. Asymmetric branches are shown in solid green. Labels (a) - (h) correspond to the saddle nodes indicated in Figure 18. Note that the asymmetric branch originating near (b) and terminating near (c) connects the $\mathcal{R}$-symmetric branches, as does that originating near (f) and terminating near (g). On the other hand the asymmetric branch originating near (c) and terminating near (f) begins and ends on the same dark blue $\mathcal{R}$-symmetric branch. The partial branches ending near (b) and originating near (g) both begin and end on the light blue $\mathcal{R}$-symmetric branch.* Right:*Solid green: the numerically observed drift speed, c, divided by $\varepsilon = 0.01$ for an asymmetric branch with the perturbation $G(u) = u_x^2$. Dotted orange: computed value of $\frac{dc}{d\varepsilon}$ along the relevant portion of the unperturbed $\kappa\mathcal{R}$-symmetric branch. Dashed green: computed value of $\frac{dc}{d\varepsilon}$ along two successive unperturbed asymmetric branches. Labels (a) - (d) correspond to the saddle nodes indicated in Figure 18.*

on the same side assuming one maximum per period π) are related by κ symmetry, and thus must have opposite signs. Turning to the four sets of asymmetric solutions along each of the asymmetric branches, two are predicted to move with positive speed (green branches) and two with negative speed of equal magnitude (purple branches), again due to their relationships via symmetry. These speeds decrease moving up the bifurcation diagram, but we note that branches come in pairs, with the speeds along the first approximately mirroring the speeds along the next one up. Of course, on each asymmetric branch, the solutions near the $\mathcal{R}$ branch will have drift speed near zero, while the solutions near a $\kappa\mathcal{R}$ branch will match the speed of the branch to which they connect.

In Figure 19, we first show the perturbed bifurcation diagram with $\varepsilon = .01$, and then compare the predictions for $\frac{\partial c}{\partial \varepsilon}$ from the right panel of Figure 18 with the drift speeds computed by direct numerical continuation. For clarity, we show the comparison for a single asymmetric branch: the drift speed c along the branch divided by $\varepsilon = 0.01$ is shown in solid green, while the predicted values of $\frac{\partial c}{\partial \varepsilon}$ computed along the relevant $\kappa\mathcal{R}$-symmetric and asymmetric branches are shown in dotted orange and dashed green, respectively. We further note that there is no relationship between distance from $\kappa\mathcal{R}$ symmetry and drift speed: while solutions along the portion of the asymmetric branch derived from the $\kappa\mathcal{R}$-symmetric branch will remain close to possessing $\kappa\mathcal{R}$ symmetry, they will have relatively large drift speeds. See also Figure 23 for plots of the distance from $\kappa\mathcal{R}$ along asymmetric branches in the planar Swift–Hohenberg system.

5.1.3 Breaking reversibility

Snaking systems without reversibility have been studied both in perturbative [16] and nonperturbative [22] regimes. Here we demonstrate that the methods described in Section 4.3 can be used to predict whether snaking

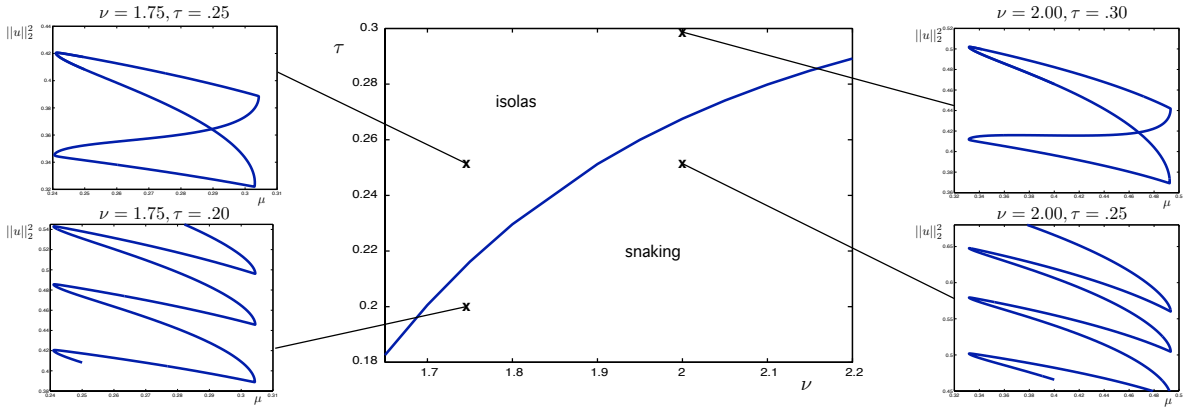

Figure 20: *Center panel: Plot of value of τ at which transition occurs as a function of ν, predicted from the unperturbed bifurcation diagram. Side panels: Partial bifurcation diagrams for (5.3) with $\varepsilon = 0.01$ and values of ν and τ as indicated above each plot and by $\times$'s in the center panel.*

or isolas will be observed. As a particular application, the system

$$u_t = -(1+\partial_x^2)^2 u - \mu u + \nu u^2 - u^3 + \varepsilon(\tau(3u_x u_{xx}^2 + u_x^2 u_{xxx}) + (1-\tau)(3u_x u_{xx})) \tag{5.3}$$

was considered in [16][3] with $\nu = 2$ and $\varepsilon = 0.3$. It was noted there that the term $3u_x u_{xx}^2 + u_x^2 u_{xxx}$ alone leads to isolas, and $3u_x u_{xx}$ alone to snaking. By repeatedly computing the full bifurcation diagram for many values of τ (with $\nu = 2$ and $\varepsilon = 0.3$ fixed), it was determined in [16] that a transition between snaking and isolas occurs for $\tau \approx 0.1$. Here we use our methods to predict the value of τ at which the switch from snaking to isolas occurs based only on the unperturbed bifurcation diagram, assuming that ε is small so that we are in a perturbative setting. We take the further step of computing this transition for a range of values of ν. Using AUTO07P, we computed the unperturbed bifurcation diagram for $\nu = 1.6$, and then continued two successive saddle nodes in μ and ν to allow computation of the transition point across a range of ν values. We then used the two saddle node solutions as described in Section 4.3 to predict the value of τ at which the transition from snaking to isolas should occur for a range of values of ν. This curve is plotted in the center panel of Figure 20. We also directly computed the bifurcation diagrams for selected values of ν and τ to confirm that they match our predictions. We note that the value of τ we compute for $\nu = 2$ is larger than that found in [16]; however, the value of ε used there is outside the perturbative regime.

5.2 Planar Swift–Hohenberg

We begin by confirming that the planar stripe and spot pattern of

$$u_t = -(1+\partial_x^2+\partial_y^2)^2 u - \mu u + \nu u^3 - u^5, \quad (x,y) \in S^1 \times \mathbb{R} \tag{5.4}$$

where $S^1 = \mathbb{R}/2L_x\mathbb{Z}$ for some $L_x > 0$, has the bifurcation structure diagrammed in Figure 13 of Section 3 above; we refer to [2] for the original computation. As discussed in [3], steady-state solutions of (5.4) can be considered as solutions to a spatial dynamical system in $U = (u, u_y, u_{yy}, u_{yyy}) \in Y := H^3(S^1) \times H^2(S^1) \times H^1(S^1) \times L^2(S^1)$, so that our analytical results detailed above remain rigorous is the planar setting.

Numerical simulations were completed in MATLAB, using a modified version of EPCONT, a predecessor of COCO [12], as in [2]. The modifications made to EPCONT include employing the Newton trust-region solver FSOLVE,

[3]We use a minus sign in front of the μu term in contrast to [16] so that the region of interest is $\mu > 0$ rather than $\mu < 0$. We also use ε instead of λ for consistency with the rest of our paper.

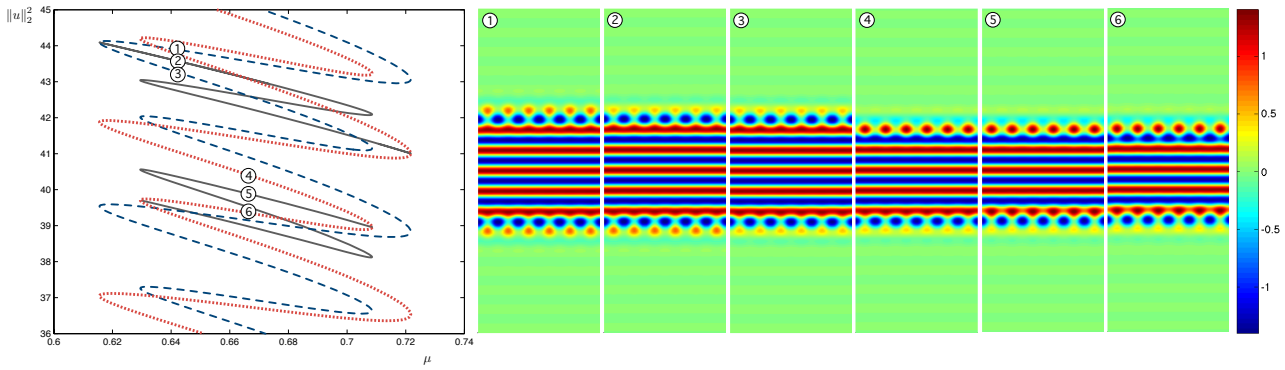

Figure 21: *Bifurcation diagram for planar stripes and spots in (5.4) (see [2]) with numbers indicating the locations of solution profiles shown at right. In the bifurcation diagram at left, $\mathcal{R}$-symmetric branches are in dashed blue, $\kappa\mathcal{R}$-symmetric branches are in dotted orange, and representative asymmetric branches are in solid gray. Profiles 1 and 3 are $\mathcal{R}$-symmetric solutions, while profile 2 is an intermediate asymmetric solution at the same parameter value, lying on a cross-connecting branch. Profiles 4 and 6 are $\kappa\mathcal{R}$-symmetric solutions, and profiles 5 is an intermediate asymmetric solution, lying on a self-connecting branch. The colorbar is the same for all solution profiles, and recalling that solutions are periodic in the x-direction, we show 6 periods for each solution.*

and projecting out the approximate translation directions in each predictor step. We use spectral differentiation matrices in the periodic x-direction, and finite differences in the y-direction. In particular, unless otherwise indicated, figures shown in this section were calculated via numerical continuation with $n_x = 8$ Fourier modes and $n_y = 800$ equidistant points on the domain $(0, \pi) \times (-50, 50)$ with Neumann boundary conditions.

Figure 21 shows the bifurcation diagram for the stripe and spot pattern of (5.4), along with selected solution profiles. Profiles 1-3 depict an asymmetric solution along with two $\mathcal{R}$-symmetric solutions existing for the same μ, and similarly profiles 4-6 show an asymmetric solution and two $\kappa\mathcal{R}$-symmetric solutions, where $\kappa : u(x) \mapsto -u(L_x - x)$. We note that both sets of solutions profiles are consistent with the gluing interpretation. We are not certain why the stripe and spot patterns possess a function z with two maxima and minima per period π; we believe these patterns arise in a transverse pitchfork bifurcation which may be related to secondary snaking, but have left this line of investigation for future work.

5.2.1 Breaking $\mathbb{Z}_2$ symmetry

As noted in Section 4.2, computations made only on an unperturbed snaking system allow us to predict the bifurcation diagram resulting from any particular perturbative term. Furthermore, having performed these calculations once, the marginal cost of analyzing the result of any number of alternative perturbations is minimal.

In Table 1 we show the results of solving for μ_ε^0 using the linear system (4.6): the calculated offset is the value of μ_ε^0, computed by solving the linear system (4.6) at a saved solution (u, μ) near each saddle node in the original $\varepsilon = 0$ bifurcation diagram. The observed offset is the difference between the original μ at the saddle node and that seen in numerical continuation for the perturbed system, divided by the ε used in the continuation. We note that finer meshes (e.g., 16 Fourier modes instead of 8) and more accurate calculation of the saddle node locations lead to somewhat higher accuracy, but since there is already some difference in the absolute value of the offsets at successive saddle nodes at distance π, e.g., between the second and sixth saddle nodes in Table 1, there are nonlinear effects which would necessitate the inclusion of higher order derivatives in ε for a complete match. Nonetheless, we see that the agreement is quite good.

For the purposes of predicting the form of the bifurcation structure, we only need the sign of the offset at the saddle nodes. In particular, to decide whether our perturbed bifurcation diagram will feature isolas, the question is simply whether adjacent inner saddle nodes are offset in the same direction. Thus we see that with the

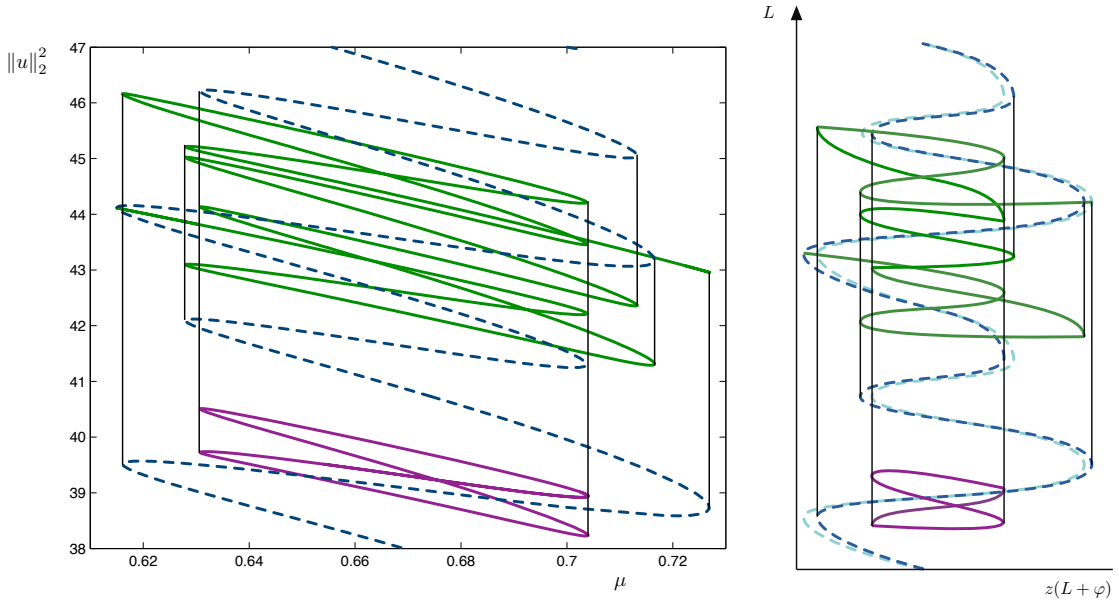

(a) *Left:* Partial bifurcation diagram for (5.5) with $\varepsilon = -0.01$, showing one of two $\mathcal{R}$-symmetric branches in dashed blue, an isola in solid purple, and a cross-connecting asymmetric branch in solid green. The cross-connecting asymmetric branch extends beyond the $\mathcal{R}$-symmetric branch as it terminates at the other $\mathcal{R}$-symmetric branch with phase $\varphi = \pi$ (not shown.) *Right:* Reproduction of the predicted bifurcation diagram from Figure 14.

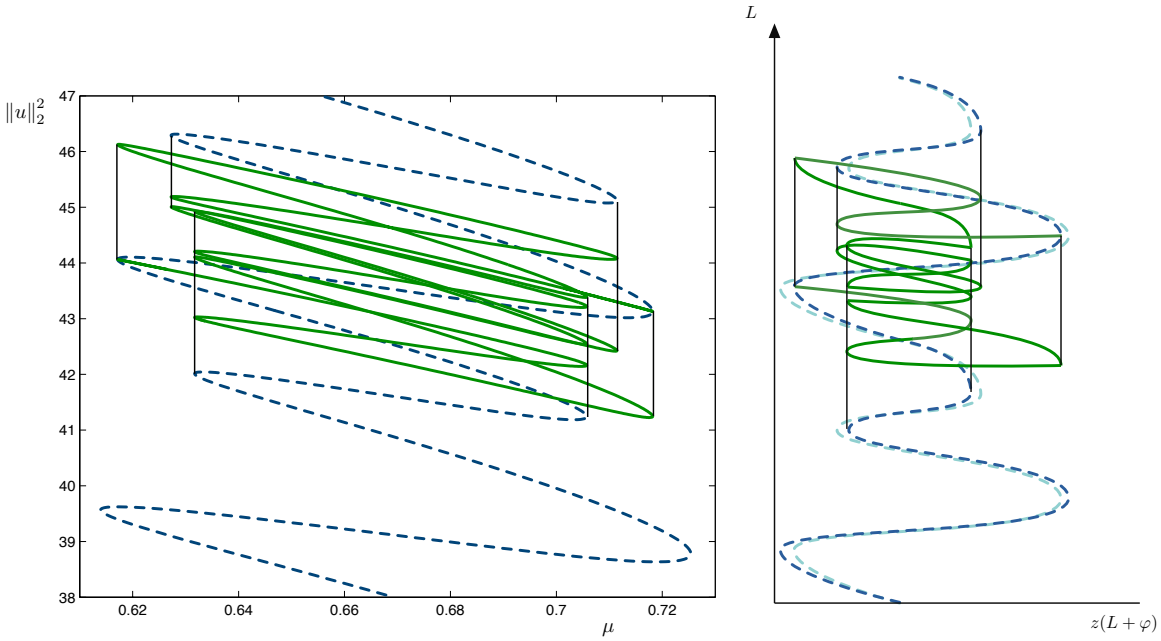

(b) *Left:* Partial bifurcation diagram for (5.6) with $\varepsilon = -0.01$, showing one of two $\mathcal{R}$-symmetric branches in dashed blue, and a self-connecting asymmetric branch in solid green. *Right:* Reproduction of the predicted bifurcation diagram from Figure 15.

Figure 22: *Comparison of numerically computed bifurcation diagrams for (5.5) and (5.6) with predicted bifurcation diagrams according to the analysis in Section 3. Vertical lines indicate the correspondence between the extrema (saddle nodes) of the $\mathcal{R}$-symmetric branch and the saddle nodes of the asymmetric branches, including the isola.*

	$G(u) = u^2$		$G(u) = u^4$	
μ at saddle node	observed offset	calculated offset	observed offset	calculated offset
0.7084	-0.4472	-0.4322	-0.2996	-0.2833
0.6156	-0.0426	-0.0470	0.1667	0.1612
0.7218	-0.4713	-0.4668	-0.3581	-0.3585
0.6294	0.1231	0.1235	-0.2331	-0.2237
0.7084	0.4361	0.4269	0.2669	0.2883
0.6156	0.0611	0.0514	-0.1508	-0.1590
0.7218	0.4833	0.4669	0.3581	0.3575
0.6294	-0.1352	-0.1228	0.2083	0.2241

Table 1: *Observed and calculated offsets over 8 saddle nodes, i.e., a full 2π period of the function z, for the planar stripe and spot pattern of (5.4), with additional perturbative term $\varepsilon G(u)$ as indicated. The values of ε used in the continuation were $\varepsilon = -0.0108$ for $G(u) = u^2$, and $\varepsilon = 0.01008$ for $G(u) = u^4$.*

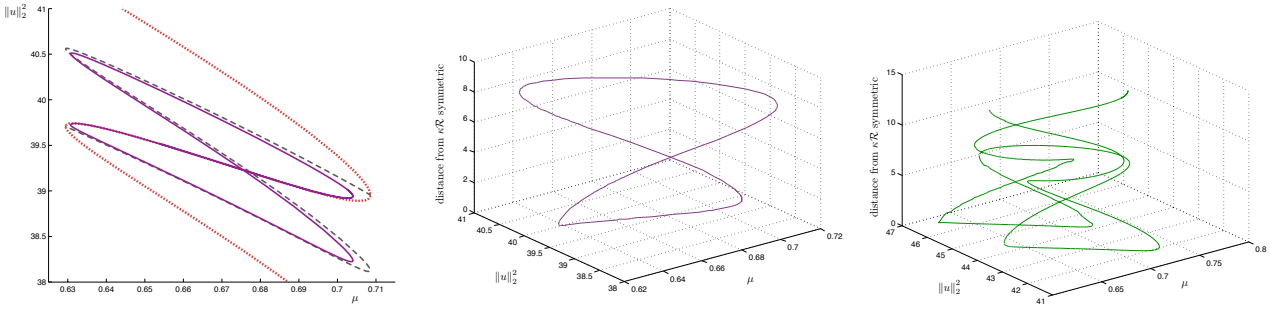

Figure 23: Left: *For comparison purposes, the isola for (5.5) with $\varepsilon = -0.01$ is shown in solid purple, along with the original ($\varepsilon = 0$) $\kappa\mathcal{R}$-symmetric branch in dotted orange, and the original ($\varepsilon = 0$) self-connecting asymmetric branch in dashed gray.* Center: *Another view of the isola, demonstrating that the symmetries are consistent with construction by combining a portion of the $\kappa\mathcal{R}$ symmetric solution branch with an asymmetric solution branch. The distance from $\kappa\mathcal{R}$-symmetry is computed as the L^2 norm of the difference between a given solution profile and the profile obtained by flipping across the y-axis, shifting by π in the x-direction, and multiplying by -1. Due to the approximate translation invariance of the solutions, this difference is minimized over translations in y.* Right: *A view of the cross-connecting branch found above, also consistent with construction via combination of $\kappa\mathcal{R}$-symmetric and asymmetric branches.*

perturbative term εu^2, i.e.,

$$u_t = -(1+\Delta)^2 u - \mu u + \nu u^3 - u^5 + \varepsilon u^2, \tag{5.5}$$

adjacent inner saddle nodes at $\mu = 0.7084$ and $\mu = 0.6156$ are offset in the same direction, and thus the perturbed bifurcation diagram will be of the form depicted in Figure 14 of Section 3. By direct numerical continuation, we find that we do indeed observe the predicted isolas bifurcating where we expect them, as shown in Figure 22(a), as well as Figure 23, left panel. We can also calculate the distance from $\kappa\mathcal{R}$ symmetry for each solution lying along the branch; doing this for the isola, we note that the middle portion is indeed almost perfectly $\kappa\mathcal{R}$ symmetric, as expected; see Figure 23, center and right panels.

On the other hand, our calculated offsets from Table 1 show that the perturbative term εu^4 causes adjacent saddle equilibria to move in opposite directions, or equivalently that one local extremum moves up while the other to moves down relative to the local extrema at distance π. Consequently this bifurcation diagram corresponds to the schematic displayed in Figure 15. In Figure 22(b) we show the results of numerical continuation on the

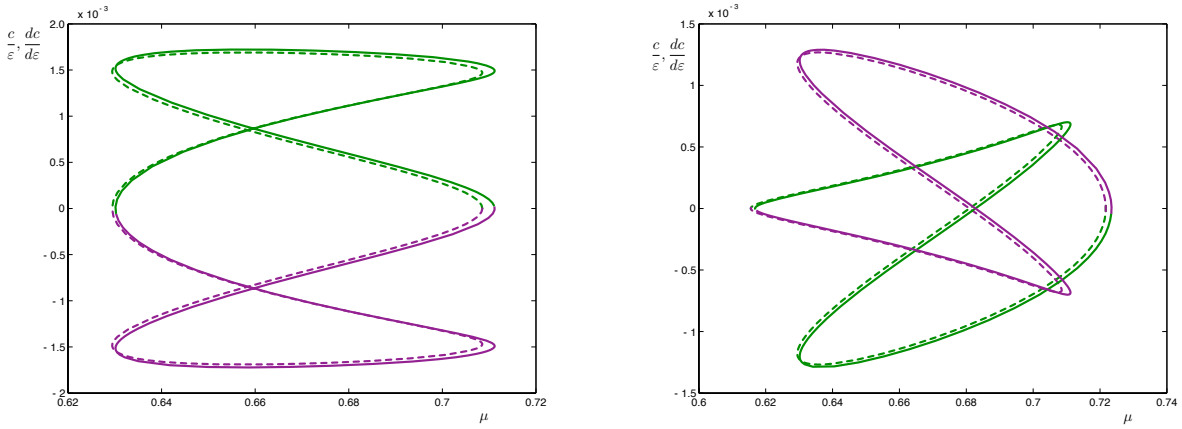

Figure 24: *Comparison of predicted and observed speeds for stripe and spot solutions to (5.7). The left panel corresponds to a self-connecting asymmetric branch, while the right panel corresponds to a cross-connecting asymmetric branch. Dashed lines indicate predicted speeds calculated from the unperturbed solution branches via (4.2), and solid lines indicate speeds observed via numerical continuation with* $\varepsilon = 0.01$*. Purple and green correspond to solutions on either side of the pitchfork bifurcations.*

planar stripe and spot patterns with perturbative term εu^4, i.e.,

$$u_t = -(1+\Delta)^2 u - \mu u + \nu u^3 - u^5 + \varepsilon u^4 \tag{5.6}$$

and see that bifurcation diagram has the anticipated form.

5.2.2 Breaking variational structure

Turning to perturbations which break the variational structure, we first consider the perturbed system

$$u_t = -(1+\Delta)^2 u - \mu u + \nu u^3 - u^5 + \varepsilon u u_x^2, \tag{5.7}$$

which breaks the variational structure of (5.4) without breaking the additional κ symmetry. We therefore expect no changes to the topological structure of the bifurcation diagram of localized stripe and spot solutions as a result of the perturbative term, and indeed see none (not shown.) However, we expect that the asymmetric solutions will begin to drift. In Figure 24 we plot the predicted and observed drift speeds for solutions along self-connecting and cross-connecting asymmetric branches; in each case we see excellent agreement.

We next consider the perturbed system

$$u_t = -(1+\Delta)^2 u - \mu u + \nu u^3 - u^5 + \varepsilon u_x^2, \tag{5.8}$$

which breaks both the variational structure of (5.4) as well as the additional κ symmetry. Using (4.7) computed along the $\mathcal{R}$-symmetric branch of stripe and spot solutions, we find that the perturbation u_x^2 will lead to the formation of isolas, and in Figure 25 we compare the drift speed observed via numerical continuation along such an isola with the speeds predicted by evaluating (4.2) along the appropriate sections of the unperturbed $\kappa\mathcal{R}$-symmetric and asymmetric branches. There is of course some difference in the speeds due to the (anticipated) branch reorganization at the outer limits of the isola, but we again see that the agreement is quite good.

6 Discussion

In the preceding, we have endeavored to advance the understanding of localized snaking structures in three respects. First, we have given a heuristic explanation, based on the "gluing" of fronts and backs, for the

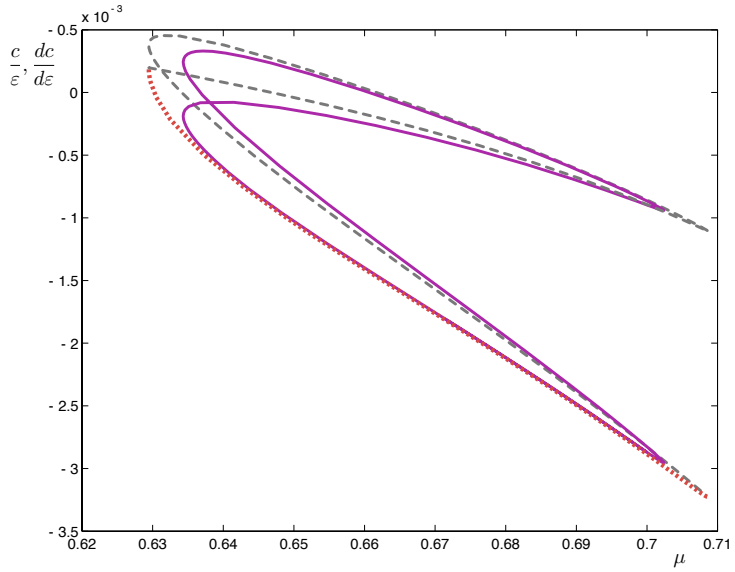

Figure 25: *Computed speed (solid purple) via numerical continuation along a newly formed isola, and predicted speeds from the appropriate original asymmetric branch (dashed grey) and relevant portion of the $\kappa\mathcal{R}$-symmetric branch (dotted orange), for the system (5.8) with $\varepsilon = 0.01$.*

appearance of formulas such as (3.1) characterizing snaking bifurcation diagrams, as seen in [3, 16, 22]. While our arguments are formal rather than rigorous, we believe the approach sheds light on various aspects of snaking bifurcation diagrams and associated solution profiles which are not immediately apparent from the rigorous spatial dynamics formulation. Further, we hope these arguments will indicate the broad applicability of the formulation given in [3].

Second, we have used the results of [3], in a similar manner to [16, 22], to predict on analytical grounds the evolution of snaking solutions and bifurcation branches in the presence of perturbative terms breaking a $\mathbb{Z}_2$ symmetry. These predictions cover the full bifurcation diagram, including the movement of symmetric branches and the reorganization of the $\kappa\mathcal{R}$-symmetric and asymmetric branches, and also explain the appearance and approximate symmetries of particular solutions lying along the new bifurcation branches. As a particular application, we have shown that given an appropriate form of the original system, isolas should form upon introduction of certain perturbations. We have verified this numerically, demonstrating that the isolas are formed exactly as expected, and possess the predicted approximate symmetries.

Finally, we have provided a new approach to the *a priori* prediction of the effects of perturbative terms in snaking systems. Given a reversible, variational snaking system possessing a $\mathbb{Z}_2$ symmetry, we have detailed methods for predicting the results of perturbations breaking any one of these structures, or combinations thereof. Our methods require knowledge only of the unperturbed solution profiles, and can be used to understand both the topological form of the resulting bifurcation diagram, and properties of particular solutions.

We have used this last method, or collection of related methods, in a number of numerical demonstrations. We have predicted and verified in both one and two-dimensional settings the effects of particular terms breaking $\mathbb{Z}_2$ symmetry. In this vein, we have also reiterated the observation of [15] on the differences in the splitting distance of the symmetric branches on the left and right, and provided an explanation based on eigenfunctions of the solutions. We have also predicted and verified the drift speeds of one and two-dimensional patterns, using perturbative terms breaking only variational structure, as well as terms simultaneously breaking both variational structure and $\mathbb{Z}_2$ symmetry. Finally, we have followed up on a particular system (5.3) from [16] involving a homotopy between two reversibility-breaking perturbative terms that lead to qualitatively different bifurcation diagrams, demonstrating how the transition between the two types may be predicted for a range of

ν values without requiring any continuation in ε.

Several areas remain for future exploration. Although it seems clear at this stage, it has not yet been shown analytically that asymmetric solutions are constructed by combining symmetric solutions, even in the one-dimensional case. Proving this rigorously will aid in addressing the stability of planar patterns, which remains an important area for further research; while some computations have been done numerically, stability in the planar case has yet to be studied analytically.

Second, while it was outlined in Section 6.4 of [3] how to extend the results given there to a system which is not spatially conservative, this approach has not been fully fleshed out. As highlighted recently by [6], studying an extended one-dimensional Swift–Hohenberg system, many questions remain for nonvariational snaking systems. We believe that our results in Section 3 hold also for nonvariational systems that are not close to having gradient structure, but some care must be taken in the rigorous formulation of this case.

Finally, localized hexagon patches (see, for example, [17]) and other fully localized structures in two or higher dimensions remain challenging phenomena where even the bifurcation structures themselves remain poorly understood. Furthermore, as highlighted recently in [23], there are strong connections between the description of localized structures via Swift–Hohenberg-type models and the transition from a fluid to crystalline state; understanding these relationships promises to be a fruitful area for ongoing work.

Acknowledgements Makrides was supported by the NSF under the IGERT grant "Reverse Ecology: Computational Integration of Genomes, Organisms, and Environments" DGE-0966060. Sandstede was partially supported by the NSF under grant DMS-0907904.

References

[1] Y. Astrov and Y. Logvin. Formation of clusters of localized states in a gas discharge system via a self-completion scenario. *Phys. Rev. Lett.* **79** (1997) 2983–2986.

[2] D. Avitabile, D. J. B. Lloyd, J. Burke, E. Knobloch and B. Sandstede. To snake or not to snake in the planar Swift-Hohenberg equation. *SIAM J. Appl. Dyn. Syst.* **9** (2010) 704–733.

[3] M. Beck, J. Knobloch, D. J. B. Lloyd, B. Sandstede and T. Wagenknecht. Snakes, ladders, and isolas of localized patterns. *SIAM J. Math. Anal.* **41** (2009) 936–972.

[4] S. Blanchflower. Magnetohydrodynamic convectons. *Phys. A* **261** (1999) 74–81.

[5] U. Bortolozzo, M. G. Clerc and S. Residori. Solitary localized structures in a liquid crystal light-valve experiment. *New J. Phys.* **11** (2009) 093037.

[6] J. Burke and J. H. P. Dawes. Localized states in an extended Swift–Hohenberg equation. *SIAM J. Appl. Dyn. Syst.* **11** (2012) 261–284.

[7] J. Burke, S. Houghton and E. Knobloch. Swift–Hohenberg equation with broken reflection symmetry. *Phys. Rev. E* **80** (2009) 036202.

[8] J. Burke and E. Knobloch. Localized states in the generalized Swift-Hohenberg equation. *Phys. Rev. E* **73** (2006) 056211.

[9] S. J. Chapman and G. Kozyreff. Exponential asymptotics of localised patterns and snaking bifurcation diagrams. *Phys. D* **238** (2009) 319–354.

[10] P. Coullet, C. Riera and C. Tresser. Stable static localized structures in one dimension. *Phys. Rev. Lett.* **84** (2000) 3069–3072.

[11] M. Cross and P. Hohenberg. Pattern formation outside of equilibrium. *Rev. Mod. Phys.* **65** (1993) 851–1112.

[12] H. Dankowicz and F. Schilder. An extended continuation problem for bifurcation analysis in the presence of constraints. *ASME J. Comp. Nonlin. Dyn.* **6** (2011) 031003.

[13] J. H. P. Dawes. The emergence of a coherent structure for coherent structures: localized states in nonlinear systems. *Philos. Trans. R. Soc. Lond. Ser. A Math. Phys. Eng. Sci.* **368** (2010) 3519–3534.

[14] M. F. Hilali, S. Metens, P. Borckmans and G. Dewel. Pattern selection in the generalised Swift-Hohenberg model. *Phys. Rev. E* **51** (1995) 2046–2052.

[15] S. M. Houghton and E. Knobloch. Swift–Hohenberg equation with broken cubic-quintic nonlinearity. *Phys. Rev. E* **84** (2011) 016204.

[16] J. Knobloch, M. Vielitz and T. Wagenknecht. Non-reversible perturbations of homoclinic snaking. *Nonlinearity* **25** (2012) 3469–3485.

[17] D. J. B. Lloyd, B. Sandstede, D. Avitabile and A. R. Champneys. Localized hexagon patterns of the planar Swift–Hohenberg equation. *SIAM J. Appl. Dyn. Syst.* **7** (2008) 1049–1100.

[18] D. Peterhof, B. Sandstede and A. Scheel. Exponential dichotomies for solitary-wave solutions of semilinear elliptic equations on infinite cylinders. *J. Differ. Eqns.* **140** (1997) 266–308.

[19] S. Pirkl, P. Ribière and P. Oswald. Forming process and stability of bubble domains in dielectrically positive cholesteric liquid crystals. *Liquid Crystals* **13** (1993) 413–415.

[20] Y. Pomeau. Front motion, metastability, and subcritical bifurcations in hydrodynamics. *Phys. D* **23** (1986) 3–11.

[21] H. Sakaguchi and H. R. Brand. Stable localized squares in pattern-forming nonequilibrium systems. *Europhys. Lett.* **38** (1997) 341–346.

[22] B. Sandstede and Y. Xu. Snakes and isolas in non-reversible conservative systems. *Dyn. Syst.* **27** (2012) 317–329.

[23] U. Thiele, A. Archer, M. Robbins, H. Gomez and E. Knobloch. Localized states in the conserved Swift–Hohenberg equation with cubic nonlinearity. *Phys. Rev. E* **87** (2013) 042915.

[24] P. D. Woods and A. R. Champneys. Heteroclinic tangles and homoclinic snaking in the unfolding of a degenerate reversible Hamiltonian-Hopf bifurcation. *Phys. D* **129** (1999) 147–170.